Applied Surface Science 585 (2022) 152693

Contents lists available at ScienceDirect

Applied Surface Science

journal homepage: www.elsevier.com/locate/apsusc

Full Length Article

Improved corrosion and wear resistance of micro-arc oxidation coatings on the 2024 aluminum alloy by incorporation of quasi-two-dimensional sericite microplates

Ke Xi [a], Hao Wu [a,*], Chilou Zhou [a], Ziyang Qi [a], Kailong Yang [a], Ricky K.Y. Fu [b], Shu Xiao [a], Guosong Wu [c], Kejian Ding [d], Guohua Chen [a], Paul K. Chu [b]

[a] Department of Mechanical and Automobile Engineering, South China University of Technology, Guangzhou 510641, PR China
[b] Department of Physics, Department of Materials Science and Engineering, and Department of Biomedical Engineering, City University of Hong Kong, Tat Chee Avenue, Kowloon, Hong Kong, China
[c] College of Mechanics and Materials, Hohai University, Nanjing 211100, China
[d] School of Science, Beijing Jiaotong University, Beijing 100044, PR China

ARTICLE INFO

Keywords:
Aluminum
Sericite
Micro-arc oxidation
Corrosion
Wear
Coatings

ABSTRACT

Although aluminum alloys are widely used in the aerospace and automotive industry, they are susceptible to local corrosion and wear during long-term service in harsh environment. In this work, micro-arc oxidation (MAO) coatings containing quasi-2D sericite microplates are prepared on the 2024 aluminum alloy, and their corrosion and wear resistance are investigated. The results reveal that the sericite-incorporated MAO sample prepared in the 15 g/L sericite electrolyte (M−15) possesses the best corrosion resistance in 3.5 wt% NaCl solution, as manifested by a corrosion current density of 2.93×10^{-10} A * cm^{-2} that is 4 orders of magnitude less than that of the 2024 Al alloy substrate. The wear resistance of MAO coating is also improved by the addition of sericite microplates, which is shown by the low wear rate and reduced coefficient of friction (~0.3) of M−15 against steel ball. Our mechanistic study reveals that the quasi-2D sericite microplates in the coatings can prevent the penetration of the corrosive media and facilitate the formation of the tribo-transfer film. The sericite-containing MAO coatings providing excellent protection to aluminum alloys under corrosion and wear conditions possess great application prospects and large commercial potential.

1. Introduction

The aim of sustainable development demands the use of lightweight materials in vehicles to reduce fuel consumption and carbon emission [1,2]. Aluminum and its alloys are widely used in the aerospace and automotive industries due to their small density, low melting point, high strength-to-weight ratio, and good formability [3]. Among them, the Al/Cu (2XXX-series) alloys are high-strength alloys often used in the aircraft industry as fuselage and door skins, dorsal fins, and propellers [4]. They are also important structural materials in vehicles as replacements for high-strength steels to reduce the weight of the body in white (BIW) [5]. However, the 2XXX-aluminum alloys are susceptible to pitting and intergranular corrosion, which greatly restricts their applications especially in highly corrosive environments [6]. Moreover, aluminum alloys are prone to adhesive wear under dry friction conditions giving rise to large friction coefficients and poor wear resistance [7]. In fact, under actual conditions, the corrosion and wear resistance of the 2XXX-series aluminum alloys are far from satisfactory [5]. Surface treatment is an effective way to improve the surface properties of aluminum alloys. Protective coatings have been prepared on Al alloys by using techniques such as anodization [8], physical vapor deposition (PVD) [9,10], electrolytic deposition [11], sol–gel deposition [12,13], laser treatment [14,15], and plasma nitriding [16]. However, these methods have various shortcomings such as high cost, complicated process, poor controllability, and difficult pretreatment.

Micro-arc oxidation (MAO), also called plasma electrolytic oxidation (PEO), is an electrolytic surface modification technology that produces thick, hard, and adherent ceramic coating on valve metals and their alloys [17–19]. However, due to severe discharge cooling and gas evolution during the MAO process, the coating formed by MAO is usually

* Corresponding author.
E-mail address: wuhao@scut.edu.cn (H. Wu).

https://doi.org/10.1016/j.apsusc.2022.152693
Received 29 October 2021; Received in revised form 27 January 2022; Accepted 28 January 2022
Available online 1 February 2022

porous and rough, which cannot effectively prevent the penetration of corrosive medium and mitigate abrasion [20,21]. The limited range of chemical compositions also hampers the wider application of MAO [22]. Recent developments have focused on adding particles to MAO coatings to seal the pores and produce new functionalities. Generally, the incorporation of micro-/nano-particles into MAO coatings can improve the tribological [23] and corrosion [24] characteristics as well as hardness and adhesion strength [25]. To obtain better corrosion resistance and wear performance, some inorganic and metal oxide particles like Al_2O_3 [26], MoO_2 [27], ZrO_2 [28,29], TiO_2 [30], ZnO [31], and SiC [32] have been proposed to adjust the composition and structure of MAO coating, although the aggregation and uneven distribution of particles in MAO coating sometimes lead to a decrease in the protective performance of the coating. The challenge of maintaining effective uptake and uniform dispersion of particles during the MAO process is still a problem that hinders practical industrial applications of particle addition in MAO [22].

Recently, two-dimensional (2D) layered materials such as graphene [33], graphene oxide (GO) [34], and MXenes [35] have been widely used in corrosion protection due to their excellent physical barrier properties. Zhu et al. [36] designed a composite coating of cationic dopamine-reduced graphene oxide ($DRGO^+$) nanosheets and epoxy with good corrosion resistance and Zhang et al. [37] prepared nacre-biomimetic GO/epoxy (NBGE) coatings by using alternative spin-coated epoxy and graphene oxide layers. Owing to their large specific surface and self-lubricating properties, the 2D layered materials are introduced into the coatings to enhance the wear resistance. Yan et al. [35] prepared MAO/$Ti_3C_2T_x$/epoxy composite coatings on the aluminum alloy to obtain good corrosion and wear resistance. Therefore, 2D layered materials are potential high-performance alternatives for metal oxide fillers and other particles. Recently, 2D materials, especially graphene oxide (GO), have also been incorporated in MAO coatings. Li et al. [38] prepared ZrO_2 coatings combined with GO by MAO, providing good corrosion and wear protection to N36 zirconium alloy. Askarnia et al. [39] revealed that adding GO into the electrolyte causes a reduction of the pores and cavities of coatings produced in the MAO process. However, 2D materials such as graphene and MXenes have disadvantages such as difficulty in preparation and high cost, making them currently uneconomical for large-scale industrial applications. Moreover, their good electrical conductivity may cause galvanic corrosion of the metal substrate, thereby accelerating metal degradation and shortening the service life of coating [40,41].

Natural materials attract special attention due to their availability, abundance, environmental-friendliness, and low cost. Sericite is a natural phyllosilicate clay mineral of fine-grained muscovite with a chemical formula of $KSi_3Al_3O_{10}(OH)_2$ [42]. As a 2:1-type layered silicate mineral, sericite comprises three-layer units containing two silicon-oxygen tetrahedrons and one aluminum/magnesium-oxygen octahedron. By grinding [43], swelling[42], heating [44], or acid activation [45,46], the raw sericite mineral can be exfoliated to obtain sericite microplates or nanoplates. Like other 2D layered materials, sericite plates possess a large ratio of lateral to axial dimension and layered structure, providing them with excellent physical barrier effect and self-lubricating properties. In addition, due to its silicate-based chemical composition, sericite plates have good electrical insulating properties, which is different from most other 2D materials. This property greatly reduces their risk of causing galvanic corrosion and makes them a potentially perfect additive to MAO coating.

In this work, the effects of adding sericite microplates on the properties of MAO coatings on aluminum alloy are studied. The sericite microplates are exfoliated from raw sericite and used to form sericite-incorporated MAO (SIM) coatings on the 2024 aluminum alloy. The anti-corrosion and anti-wear properties of the SIM coatings are evaluated, and the related mechanisms are also investigated and discussed.

2. Experimental details

2.1. Preparation of MAO coatings

2024 Al alloy (3.9% Cu, 1.2 % Mg, 0.6% Mn, balance Al, wt%) samples with dimensions of 40 × 25 × 2 mm were used as the substrate. Prior to MAO, the specimens were sequentially ground and polished with 400, 1200, 2000 grit silicon carbide paper, cleaned ultrasonically in acetone and ethanol for 10 min, and dried in cool air. The natural sericite powder (800 mesh, obtained from Wanqiao Mica Inc., Chuzhou, China) was pretreated according to the following procedures. The natural sericite was heated to 800 °C in a muffle furnace for 1 h, and then 15 g of the sericite powder were dispersed in 500 mL 5.0 mol/L HNO_3 at 95 °C, stirred for 5 h, filtered and washed with deionized water at 80 °C for several times until the pH was 7, and then dried at 80 °C. In order to ensure dispersion of the sericite, the electrolytes with different concentrations of sericite were stirred and ultrasonicated for 2 h before MAO.

MAO was performed on a custom system comprising a DC pulsed power supply (Protech Advanced Materials Ltd., Guangzhou) and a stainless steel container as the cathode. A cooling system and mechanical stirrer were utilized to keep the electrolyte temperature below 55 °C. The electrolyte was prepared by dissolving 30 g/L $Na(PO_3)_6$ in deionized water and then adding different concentrations of as-treated sericite powder from 0 to 15 g/L. The mixture was stirred and sonicated to obtain a steady electrolyte. The MAO processing was conducted using the constant current mode with the current density of 10 A/dm^2, power frequency of 400 Hz, and duty cycle of 30% for 10 min. After treatment, the MAO-coated sample was taken out from the electrolyte, washed with deionized water and ethanol, and dried by air flow. The samples were labeled M, M−5, M−10, and M−15, respectively, according to the concentrations of sericite.

2.2. Materials characterization

The high-resolution transmission electron microscopy (HR-TEM, FEI, Technai F20, USA) was employed to characterize the microstructure of the sericite microplates. The X-ray diffraction patterns of untreated and as-treated sericite powders were obtained on an X-ray powder diffractometer (XRD, PANalytical X'pert Powder, Netherlands) employing Cu K_α radiation ($\lambda = 0.15418$ nm). The XRD data were collected in the 2θ range from 10° to 80° at a scanning rate of 12°/min and step size of 0.013°. The surface and cross-sectional morphologies and elemental compositions of the coatings were characterized by field-emission scanning electron microscopy (FE-SEM, Carl Zeiss, SUPRA® 55, Germany), and the elemental distribution was determined by energy-dispersive X-ray spectroscopy (EDS). The composition was determined by grazing-incidence X-ray diffraction (GIXRD, Rigaku SmartLab, Japan) with Cu K_α radiation ($\lambda = 0.15418$ nm) at an incidence angle of 1°. The GIXRD data were collected in the 2θ range of 10°–90° at a scanning rate of 2°/min and step size of 0.02°. The Vickers hardness of different coatings was measured by using a Vickers hardness tester (HMV-2 T, Shimadzu, Japan) with a load of 200 g.

2.3. Corrosion evaluation

The corrosion resistance of the 2024 aluminum alloy and MAO-treated samples were evaluated through electrochemical tests and immersion tests in 3.5 wt% sodium chloride solution at room temperature (25 °C). The electrochemical tests were carried out on the electrochemical workstation (Reference 600+, Gamry, USA) with the standard three-electrode cell composed of a saturated calomel electrode (SCE) as the reference electrode, a platinum mesh electrode as the counter electrode, and the sample with an exposed area of 1 cm^2 as the working electrode. After stabilization for 30 min at the open-circuit potential (OCP), potentiodynamic polarization (POL) was conducted from − 0.25

V to 0.75 V (vs. OCP) at a scanning rate of 1 mV/s. The potential was scanned from the cathodic to the anodic regions to acquire the polarization curves. The corrosion current densities (i_{corr}) and corrosion potentials (E_{corr}) were calculated by Tafel extrapolation. Electrochemical impedance spectroscopy (EIS) was obtained after immersion for different times to investigate the electrode/solution interface after stabilization for 30 min. The data were recorded from 0.1 MHz to 0.1 Hz with a sinusoidal perturbing signal of 20 mV at the open-circuit potential. The EIS data were fitted numerically by using the Gamry Echem Analyst software. All the electrochemical tests were conducted at least three times to ensure repeatability.

Immersion tests were performed to investigate the corrosion behavior of different samples. The samples were immersed in 3.5 wt% NaCl solution at room temperature for 0, 3, 5, 7, and 14 days. After immersion in 3.5 wt% NaCl at room temperature for 0, 3, 5, 7, and 14 days, the samples were taken out, rinsed with water and ethanol, and dried by flowing air. The surface morphology after the immersion test was observed by FE-SEM and confocal laser scanning microscopy (CLSM, VK-X200, KEYENCE, Japan) and the elemental composition was determined by EDS.

2.4. Tribological evaluation

The tribological properties of the coatings were evaluated by ball-on-flat friction experiments on the UMT-3 micro-tribometer (Bruker, Campbell, CA, USA) with a GCr15 steel ball (Ø = 6 mm) as friction pair. The tribological test was carried out in rotational sliding mode under dry conditions. The normal load, wear radius, sliding speed, and time were set to 2 N, 3 mm, 200 r/min, and 600 s, respectively. The coefficient of friction (COF) was recorded over time at a data acquisition rate of 100 Hz. The surface morphology of wear tracks on samples was examined by FE-SEM and 3D optical profilometry (UP Dual Model, Rtec, USA), and the elemental composition was determined by EDS. The worn surfaces of the counterpart balls were observed by optical microscope.

3. Result and discussion

3.1. Characterization of sericite microplates

The composition and microstructure of sericite before and after pretreatment are characterized. Fig. 1(a) shows the wide-angle XRD patterns of the raw and as-treated sericite and the inset shows the small-angle XRD patterns from 1° to 10°. The diffraction peaks are consistent with muscovite (JCPDS 07–0032) and quartz (JCPDS 01–079-1910). Most peaks remain after the heat and acid treatment suggesting no phase transformation after pretreatment [45]. The spectra show decreased intensities for peaks such as (002) and (004) after the heat and acid treatment, suggesting that the sericite lattices dissociate along the (002) direction [47–49]. The (002) peak shifts from 8.85 to 8.74 after pretreatment due to the enlarged interlayer spacing from 9.98 Å to 10.11 Å. The results indicate that the lamellar structure of sericite is separated after pretreatment. As shown in Fig. 1(b), the particle size of the sericite plates ultrasonically dispersed in deionized water is found to decrease from 3585.96 nm to 1843.46 nm and the Gaussian-like distribution of the particle size is sharper after pretreatment. This phenomenon is also revealed by XRD that the sericite lamellae are exfoliated from the original structure. The zeta-potential (ζ) distribution (Fig. 1c) shows that the average ζ value of the sericite plates changes from + 8.96 mv to −27.89 mv, suggesting that the surface electrical charge of the sericite microplates becomes negative and increases after pretreatment.

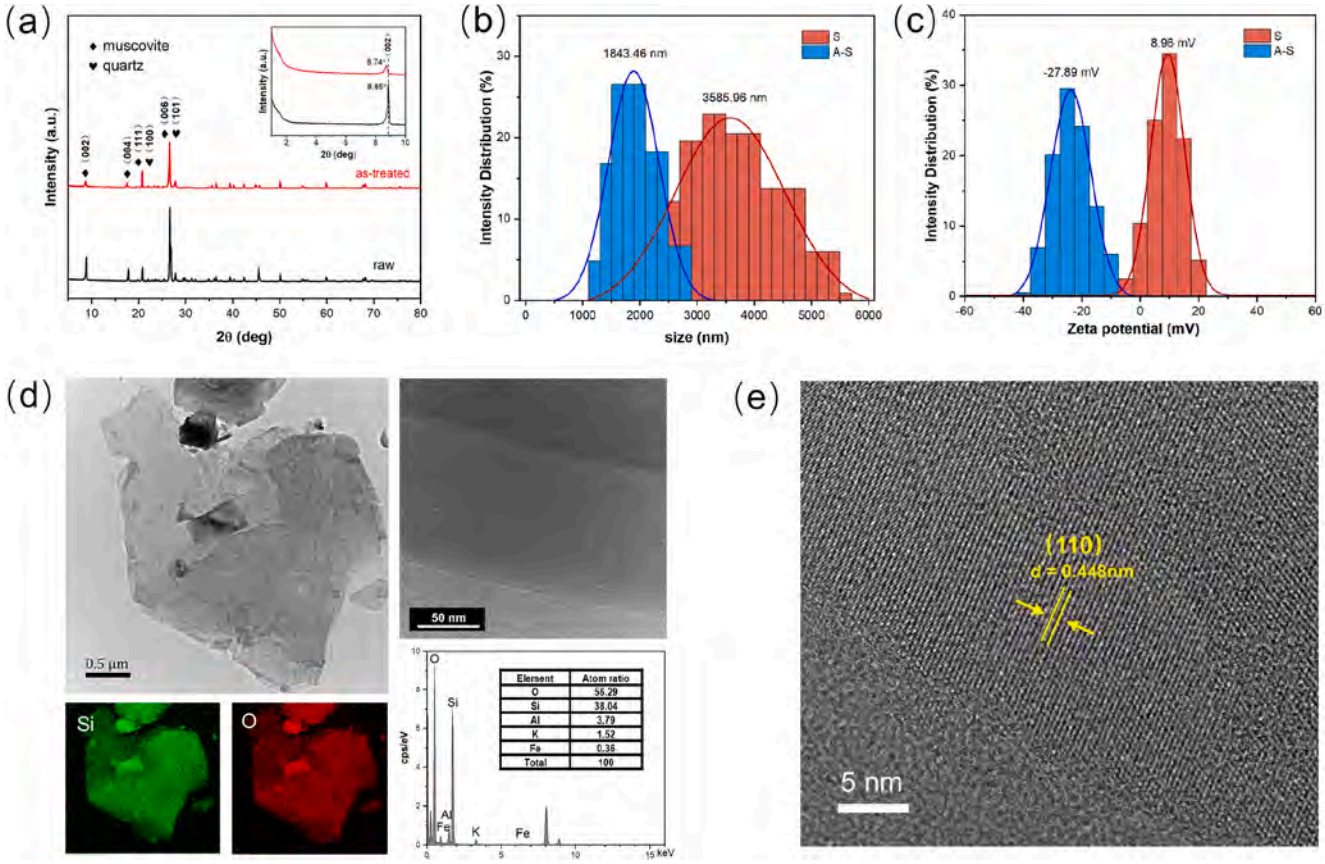

Fig. 1. (a) Wide-angle and small-angle X-ray diffraction (XRD) patterns; (b) Particle size distributions and (c) Zeta potential distributions of sericite before (S) and after pretreatment (A-S); (d) Low-resolution TEM micrograph of a fragment from sericite after modification with the inset on the left bottom showing the EDS maps of different elements and insets on the right-bottom showing the EDS spectrum of the related area; (e) High-resolution TEM micrograph taken from area (d).

Generally, a higher zeta potential of particles indicates higher stability of the particle-liquid system. The sericite microplates with higher ζ value can be better dispersed in the electrolyte, which is conducive to stable discharge during MAO and uniform incorporation of particles into the coating. The relationship between ζ and electrophoretic mobility (U) is expressed by Smoluchowski's equation [50]:

$$U = \frac{\varepsilon_w \varepsilon_0 \zeta}{\eta}$$

where U is the electrophoresis force of the dispersed particles relative to a fluid under the influence of electric field, ε_w is the dielectric constant of the dispersion medium, ε_0 is the permittivity of free space, η is the viscosity of the dispersion medium, and ζ is the zeta potential. The negative charge of the particles facilitates electrophoretic movement during positively charged MAO and incorporation into the MAO coating [22].

The microstructure of the sericite plates is further characterized by transmission electron microscopy (Fig. 1d). The low-resolution TEM image of a sericite-plate fragment shows a typical multi-layer lamellar structure of quasi-2D materials. EDS reveals that the sericite plates are composed of Si and O with small amounts of K, Al, and Fe. The high-resolution TEM image (Fig. 1e) shows the edge area of a sericite lamella on a single layer of sericite structure. The lattice fringes show the (1 1 0) plane of muscovite, suggesting successful exfoliation of the sericite microplates. These results show that negatively charged sericite microplates are obtained after the pretreatment and exfoliation of the raw sericite. The particle size decreases and particle dispersibility increases as well.

3.2. Voltage-Time response

Fig. 2 shows the galvanostatic dependence of the positive voltage on the MAO time in electrolytes with different concentrations of sericite. The MAO samples prepared in 0 g/L, 5 g/L, 10 g/L, 15 g/L are denoted as M, M−5, M−10, and M−15, respectively. At a current density of 10 A/dm^2, sericite has a relatively minor influence on the voltage–time response and the three curves overlap to a large extent. It is common to separate the MAO process into three stages [51–53]. In stage 1, similar to conventional anodic oxidation, the voltage goes up sharply to about 370–380 V in the initial 50 s, leading to the formation of the initial oxide film on the surface of the 2024 Al alloy [54]. At the beginning of stage 2, the slope of the voltage–time curve decreases after about 50 s suggesting a barrier effect of the initial oxide films. Gas liberation can be observed shortly before the start of discharges. The sparks start to emerge and move on the sample. The voltage suddenly increases by ~ 80 V due to the breakdown of the initial oxide film by the micro-discharge sparks [31]. The breakdown voltages increase with sericite concentrations in the electrolytes. This may be due to the deposition of negatively charged sericite plates on the substrate at the positive voltage. In stage 3, the voltages continue to rise steadily and slowly. Bright and slow-moving sparks can be observed from the sample surface with increasing intensity. The electrical resistance increases as the oxide layer becomes thicker [55]. The surface discharge moves randomly on the surface and creates different morphologies [56]. The overall trend of the V-T curves and electrolyte conductivity is not affected by the addition of sericite, but the voltage improves slightly with sericite concentrations in the electrolyte. When the sericite concentration increased to 20 g/L or higher, the dispersibility of sericite in the electrolyte became poor and the discharge became unstable, causing localized "burning" effect on the samples. Hence, in our experiments, the highest concentration of sericite in the electrolyte is 15 g/L.

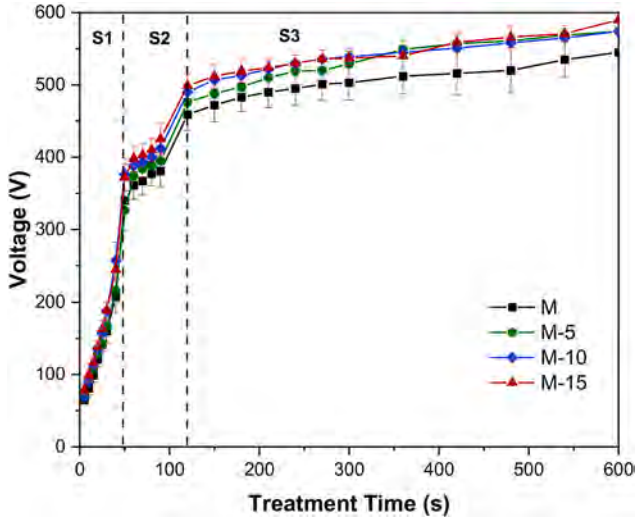

Fig. 2. Voltage-time response during the MAO process in the constant current mode.

3.3. Morphology and phase composition of the coatings

The influence of sericite on the composition and microstructure of the MAO coatings is evaluated. The phases of the MAO coatings are shown in the GIXRD patterns (Fig. 3a). The broad peak between 2θ of 20°~35° indicates the amorphous phases of alumina and aluminum phosphate [31]. For crystalline alumina, the peaks at 19.5°, 31.9°, 37.5°, 39.5°, 45.7° and 66.9° originate from γ-Al_2O_3 (alumina, JCPDS NO. 10–0425), and the peaks at 25.6°, 35.1°, 37.8°, and 61.4° refer to α-Al_2O_3 (alumina, JCPDS NO. 46–1212). The weak peaks at 20.1°, 21.5°, and 22.8° are associated with $AlPO_4$ (aluminum phosphate, JSPDS NO. 50–0303), which is generated by the side reactions between the hydrolysate of $(NaPO_3)_6$ and Al^{3+} anions [57]. The diffraction peak at 26.5° provides evidence of sericite (JSPDS NO. 47–1144) in the coatings. Fig. 3(b) shows the elemental concentrations of the MAO coatings prepared in electrolytes with different concentrations of sericite. The MAO coating with no sericite contains O, Mg, Al, and P, whereas the sericite-incorporated MAO coatings consist of O, Mg, Al, P, and Si. The atomic concentrations of Si increase with sericite concentration. M−15 possesses the largest Si concentration of 2.14% with an Al/Si ratio of ~ 14:1. The concentrations of Mg and P decrease slightly with the addition of sericite.

Fig. 3(c-f) exhibit the SEM images of the coatings prepared with different electrolytes. All the samples have the typical porous and rough microstructure and even some micro-cracks on the surface. The micropores are created by molten oxide and gas bubbles emitted from the micro-arc discharge channels [58], whereas micro-cracks are formed by thermal stress due to rapid solidification of molten oxide in the relatively cool electrolyte [59]. Fig. 3(d-f) show the coatings prepared in $Na(PO_3)_6$ solutions with 5, 10, 15 g/L sericite microplates. With the help of EDS mapping of Si, some sericite microplates located in the near-surface layer of coatings are marked in the insets of Fig. 3(d-f). It can be seen that part of the microplates tends to be distributed near or in the micropores, which may be due to the discharge-solidification process that brings these microplates into the coatings.

Fig. 4 displays the cross-sectional SEM images and EDS maps of the MAO samples, and there is a wavy interface between the coating and substrate. As the concentration of sericite increases, the Si element distribution in the coating gradually changes from being enriched in the surface layer to being uniformly distributed throughout the coating, which can be possibly due to the electrophoretic effect of sericite microplates during MAO treatment. According to characterization results, it is confirmed that sericite microplates are successfully introduced and evenly embedded in the MAO coatings. However, the overall morphology and structure of the coating did not change dramatically with the addition of sericite. As shown in Table.1, the average coating thickness increases slightly, and the surface roughness (R_a) decreases slightly as the content of sericite increases. Notably, the Vickers

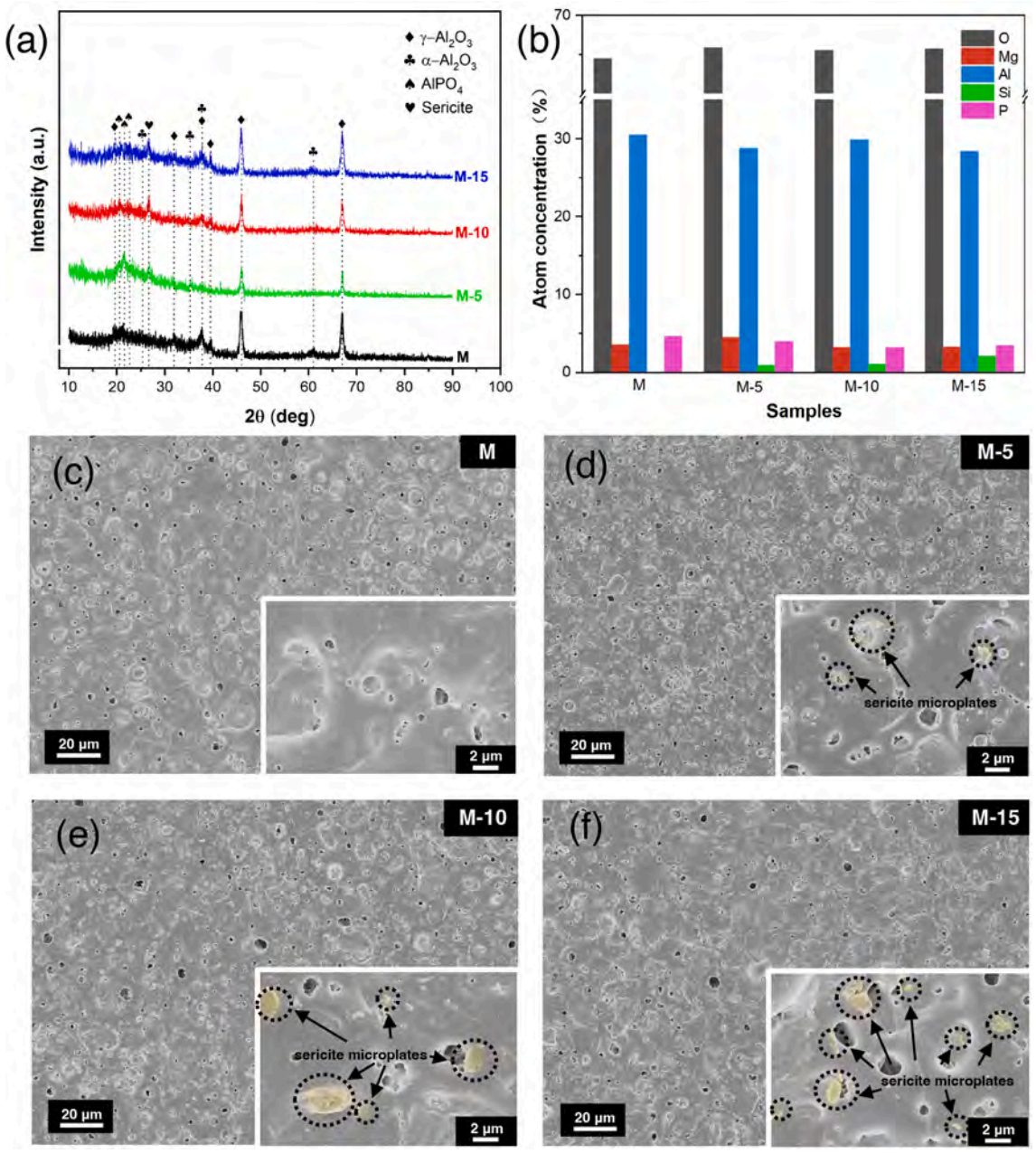

Fig. 3. (a) Grazing-incidence X-ray diffraction (GIXRD) spectra; (b) Elemental concentrations of the MAO coatings prepared in electrolytes containing different concentrations of sericite determined by EDS; (c–f) SEM images showing the surface morphology of the MAO coatings prepared in electrolytes containing (c) 0 g/L, (d) 5 g/L, (e)10 g/L, and (f)15 g/L sericite.

hardness of the MAO coating increases from 520.8 HV to 610.3 HV when the sericite concentration in electrolyte increases from 0 to 15 g/L, indicating that the incorporation of sericite improves the mechanical property of the MAO coating.

3.4. Electrochemical corrosion tests

Fig. 5(a) shows the potentiodynamic polarization (POL) curves of the samples in 3.5 wt% NaCl. The corrosion potentials (E_{corr}) and corrosion current densities (i_{corr}) derived from the Tafel region in the cathodic polarization curves by Tafel extrapolation are listed in Table 2 and Fig. 5 (b), respectively. The polarization curves shift to the left and upward as the sericite contents increase, indicating more positive corrosion potentials and lower corrosion current densities. E_{corr} moves to the noble side from − 0.571 V to − 0.464 V, and i_{corr} continuously decreases from 1.77×10^{-8} A * cm^{-2} to 2.93×10^{-10} A * cm^{-2} when the sericite concentration increases from 0 g/L to 15 g/L. In particular, M−15 shows the smallest i_{corr}, which is about 2 orders of magnitude lower than that of M and 4 orders of magnitude lower than that of the 2024 Al substrate. Generally, more positive E_{corr} and lower i_{corr} correspond to lower corrosion rate and better corrosion resistance [37,60]. Therefore, the corrosion resistance of the MAO coating is improved by the incorporation of sericite microplates.

Electrochemical impedance spectroscopy is employed to investigate the corrosion behavior of the samples. Fig. 6(a-c) depict the Nyquist and bode plots of 2024 Al, M, M−5, M−10, and M−15 after immersion in 3.5 wt% NaCl for 30 min. As shown by the Nyquist plot (Fig. 6a), the capacitive loop of 2024 Al is significantly enlarged after MAO treatment. The bode impedance plot (Fig. 6c) also shows that the impedance modulus (|Z|) has improved after MAO because the MAO coating

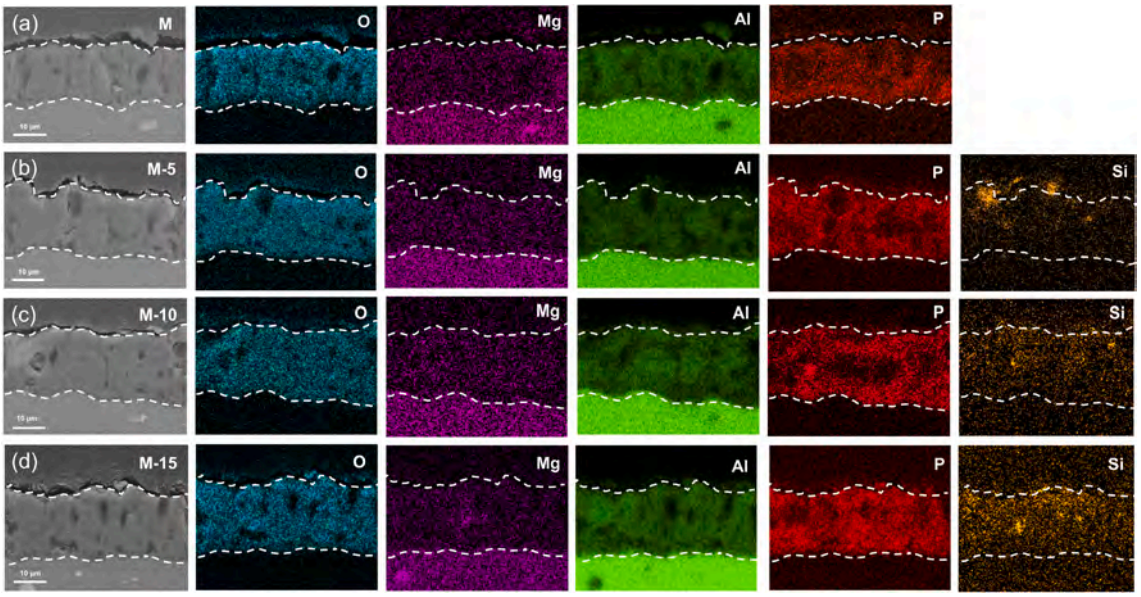

Fig. 4. Cross-sectional SEM images of the MAO coatings formed in electrolytes containing different concentrations of sericite together with the EDS maps of different elements.

Table 1
Average thickness, surface roughness (R_a) and Vickers hardness ($HV_{0.2}$) of the MAO coatings prepared in electrolytes with different sericite concentrations.

Sericite concentration (g/L)	0	5	10	15
Average thickness (μm)	16.1	17.8	18.2	18.9
R_a (μm)	2.70 ± 0.11	2.95 ± 0.12	2.56 ± 0.17	2.08 ± 0.10
Vickers hardness ($HV_{0.2}$)	520.8 ± 52.6	537.6 ± 36.9	578.5 ± 43.3	610.3 ± 43.1

isolates and protects the 2024 Al substrate from the corrosive environment [61]. Moreover, there is an overall trend that both the diameter of the capacitive loop and $|Z|$ value increase with increasing amounts of sericite. Here, the low-frequency impedance at 0.1 Hz ($|Z|_{0.1Hz}$) is used to estimate the overall corrosion resistance of the MAO coatings. Generally, a larger $|Z|_{0.1Hz}$ indicates better corrosion resistance [61–63] and the $|Z|_{0.1Hz}$ values at 30 min of M, M−5, M−10, and M−15 are 7.101×10^5 Ohm·cm^2, 2.559×10^6 Ohm·cm^2, 6.07×10^6 Ohm·cm^2, 1.116×10^7 Ohm·cm^2, respectively, thus indicating that the corrosion resistance increases with the addition of sericite.

The EIS data are fitted numerically by using equivalent circuits. Among these circuits, constant phase element (CPE) is used to represent the non-ideal capacitor as shown below:

$$Y = Y_0(j\omega)^n$$

which Y_0 and n are the admittance constant and empirical exponent,

Table 2
E_{corr}, i_{corr}, and β_c of different samples in 3.5 wt% NaCl solution calculated from the polarization curves.

Sample	E_{corr} (V vs. SCE)	i_{corr} (A*cm^{-2})	β_c (V/decade)
2024	−0.615 ± 0.015	$(1.29 \pm 0.10) \times 10^{-6}$	−0.523 ± 0.002
M	−0.571 ± 0.016	$(1.77 \pm 0.27) \times 10^{-8}$	−0.406 ± 0.034
M−5	−0.548 ± 0.021	$(3.19 \pm 0.20) \times 10^{-9}$	−0.605 ± 0.022
M−10	−0.465 ± 0.039	$(1.43 \pm 0.13) \times 10^{-9}$	−0.611 ± 0.008
M−15	−0.464 ± 0.021	$(2.93 \pm 0.25) \times 10^{-10}$	−0.262 ± 0.008

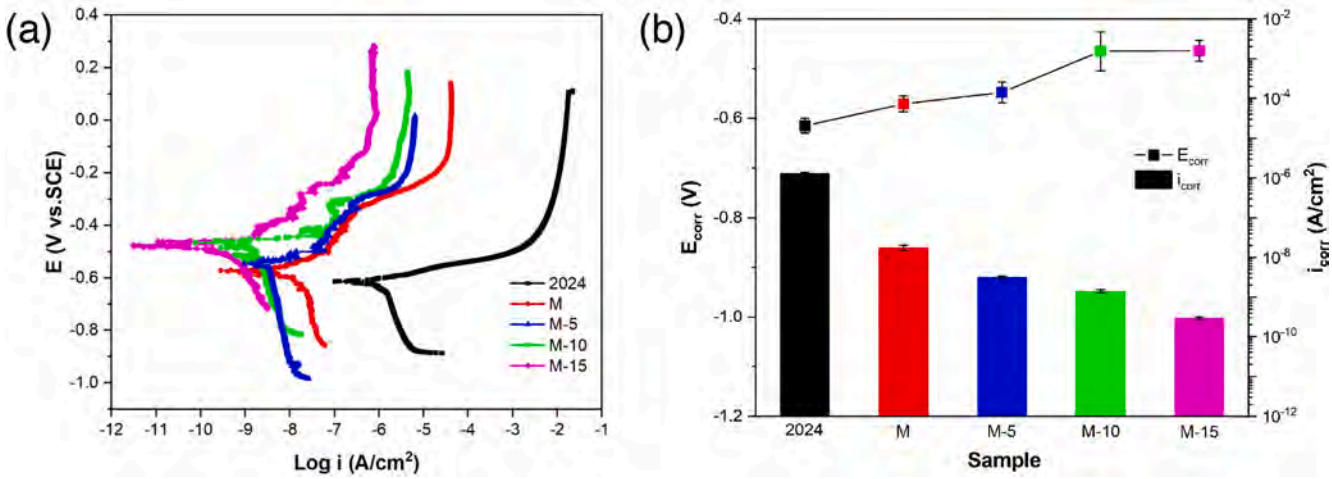

Fig. 5. (a) Potentiodynamic polarization curves of the 2024 substrate and MAO samples after immersion in 3.5 wt% NaCl solution for 30 min; (b) Comparison of the corrosion potentials (E_{corr}) and corrosion current densities (i_{corr}) calculated from the polarization curves.

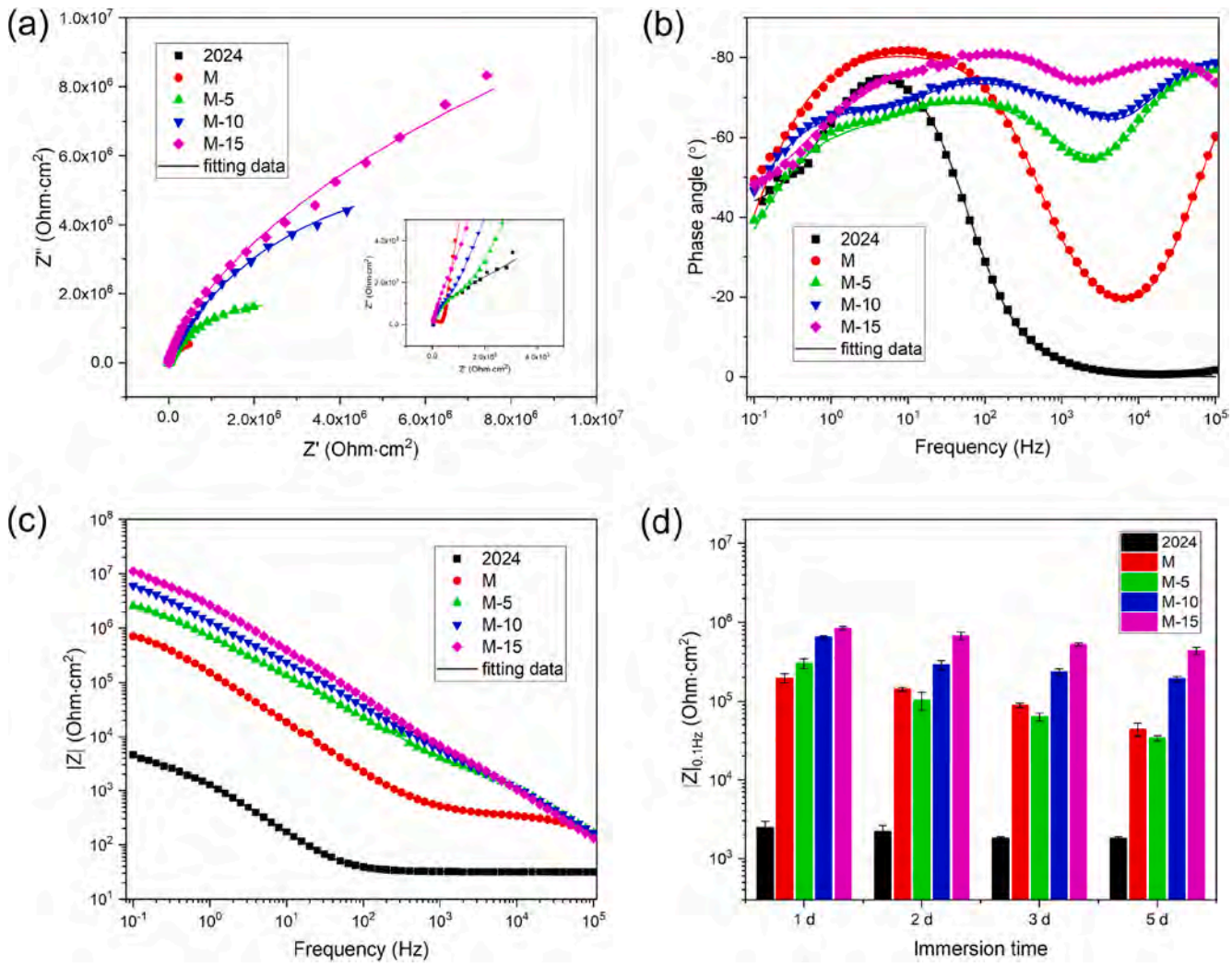

Fig. 6. (a-c) Nyquist and bode plots for the 2024 substrate, M, M−5, M−10, and M−15 after immersion in 3.5 wt% NaCl for 30 min; (d) The $|Z|_{0.1Hz}$ values for 2024 substrate, M, M−5, M−10, M−15 after immersion in 3.5 wt% NaCl for 1, 2, 3, 5 days.

respectively [64,65]. Generally, the higher frequency behavior is related to the surface film and charge transfer, and the lower frequency behavior is associated with mass transfer [66–68]. The Nyquist plot and the frequency-phase angle curve of the 2024 aluminum alloy suggest two time constants. As shown in Fig. 7(a), an equivalent circuit of R_s (CPE_{dl} (R_{ct} W_d)) is established to fit the EIS data of the 2024 alloy sample,

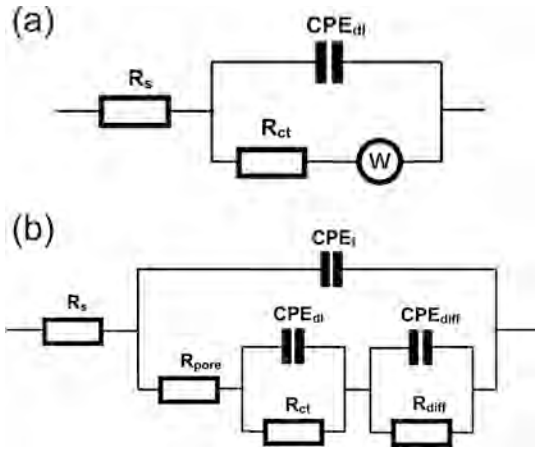

Fig. 7. (a, b) Equivalent circuits for fitting the EIS data.

where R_s represents the solution resistance, CPE_{dl} and R_{ct} stand for the capacitance of the electric double layer at the low-frequency area and charge transfer resistance in the Faradic process, respectively, and W_d represents the Warburg impedance diffusion process during corrosion. For these MAO samples, three time constants are observed from the Nyquist and bode phase angle plots. Based on the previous literatures [69,70], the equivalent circuit R_s (CPE_f (R_{pore} ((CPE_{dl} R_{ct})(CPE_{diff} R_{diff})))) (Fig. 7b) is used to simulate the EIS data of M, M−5, M−10, and M−15 samples. In this model, R_s, CPE_{dl}, and R_{ct} remain the same meaning as the previous ones. CPE_f represents the capacitance of the MAO coating and R_{pore} stands for the total resistance of pore and defects in the MAO coating. CPE_{diff} represents the capacitance pertaining to the diffusion process and R_{diff} denotes the relevant resistance.

The fitted results of EIS are presented in Tables 3. For all the tested samples, R_{pore} increases with the addition of sericite, indicating that sericite incorporation inhibits the penetration of corrosive media through MAO coating and improves the barrier effect of the coating. The decrease in $Y_{0\,f}$ of the samples from M to M−15 may be attributed to the non-conductive barrier layer formed by sericite microplates. The significant improvement of R_{ct} and R_{diff} with sericite addition reflects that the corrosion reactions at the substrate/electrolyte interface are retarded, and the decrease of the $Y_{0\,dl}$ and $Y_{0\,diff}$ also indicates much lower corrosion activity of the substrate [37]. The polarization resistance (R_p) is estimated by the sum of R_{pore}, R_{ct}, and R_{diff}. According to our

Table 3
Fitted EIS results of different samples after immersion in 3.5 wt% NaCl solution for 0.5 h based on the corresponding equivalent circuit models.

	2024 Al	M	M−5	M−10	M−15
R_s (Ohm·cm^2)	32.06	10.65	9.26	13.97	16.27
$Y_{0\ f}$ (Ohm^{-2}·cm^{-2}·S^{-n})	–	4.68×10^{-8}	3.66×10^{-8}	3.25×10^{-8}	2.27×10^{-8}
n_f	–	0.8741	0.9109	0.9032	0.9067
R_{pore} (Ohm·cm^2)	–	393.2	2.94×10^{3}	3.86×10^{3}	1.59×10^{4}
$Y_{0\ dl}$ (Ohm^{-2}·cm^{-2}·S^{-n})	1.43×10^{-3}	1.24×10^{-6}	7.55×10^{-7}	7.72×10^{-8}	1.15×10^{-8}
n_{dl}	0.2386	0.9101	0.8836	0.8253	0.8256
R_{ct} (Ohm·cm^2)	2.11×10^{3}	2.07×10^{3}	1.03×10^{5}	9.26×10^{5}	5.86×10^{6}
$Y_{0\ diff}$ (Ohm^{-2}·cm^{-2}·S^{-n})	–	9.99×10^{-5}	3.15×10^{-6}	1.82×10^{-6}	5.01×10^{-7}
n_{diff}	–	0.8125	0.7825	0.7075	0.7662
R_{diff} (Ohm·cm^2)	–	1.23×10^{6}	4.39×10^{6}	1.33×10^{7}	2.43×10^{7}
W_d(S·s$^{1/2}$)	3.29×10^{-4}	–	–	–	–
χ^2	4.52×10^{-4}	2.04×10^{-4}	1.67×10^{-3}	3.39×10^{-4}	7.66×10^{-4}

result, the M−15 sample shows the highest R_p, implying the best corrosion resistance, which is also consistent with the POL results.

To study the long-term corrosion behavior, EIS is carried out after exposing all samples to 3.5 wt% NaCl for 1, 2, 3 and 5 days. Fig.S1 shows the Nyquist and bode plots of all samples after 1, 2, 3, and 5 days of immersion. The low-frequency impedance modulus ($|Z|_{0.1Hz}$) was used to evaluate the variation of overall corrosion resistance. As seen from Fig. 6(d), the $|Z|_{0.1Hz}$ decreases with the increase of immersion time, indicating that the overall corrosion resistance decreases during immersion, which may be due to the diffusion of corrosive media and the propagation of the corrosion process. However, the addition of sericite alleviates the deterioration tendency of corrosion resistance with increasing immersion time. Compared with the M sample, the $|Z|_{0.1Hz}$ of M−5 declines more obviously after 2 days of immersion. However, for M−10 and M−15, the decline trend of $|Z|_{0.1Hz}$ with immersion time is obviously slowed down. After 1, 2, 3, and 5 days of immersion, the $|Z|_{0.1Hz}$ of M−15 sample was increased by 325.5%, 374.9%, 485.9%, and 881.1%, respectively, compared with that of the M sample. Therefore, the SIM coating with higher sericite content offers better long-term corrosion protection.

3.5. Immersion tests

Fig. 8(a) depicts the pictures of the samples after continuous immersion in 3.5 wt% NaCl for 0, 3, 5, 7, and 14 days. After immersion for 3 days, noticeable discoloration and corrosion damage appear from the 2024 substrate. Localized corrosion begins to occur in a relatively small area on M on the third day and gradually spreads to almost the entire

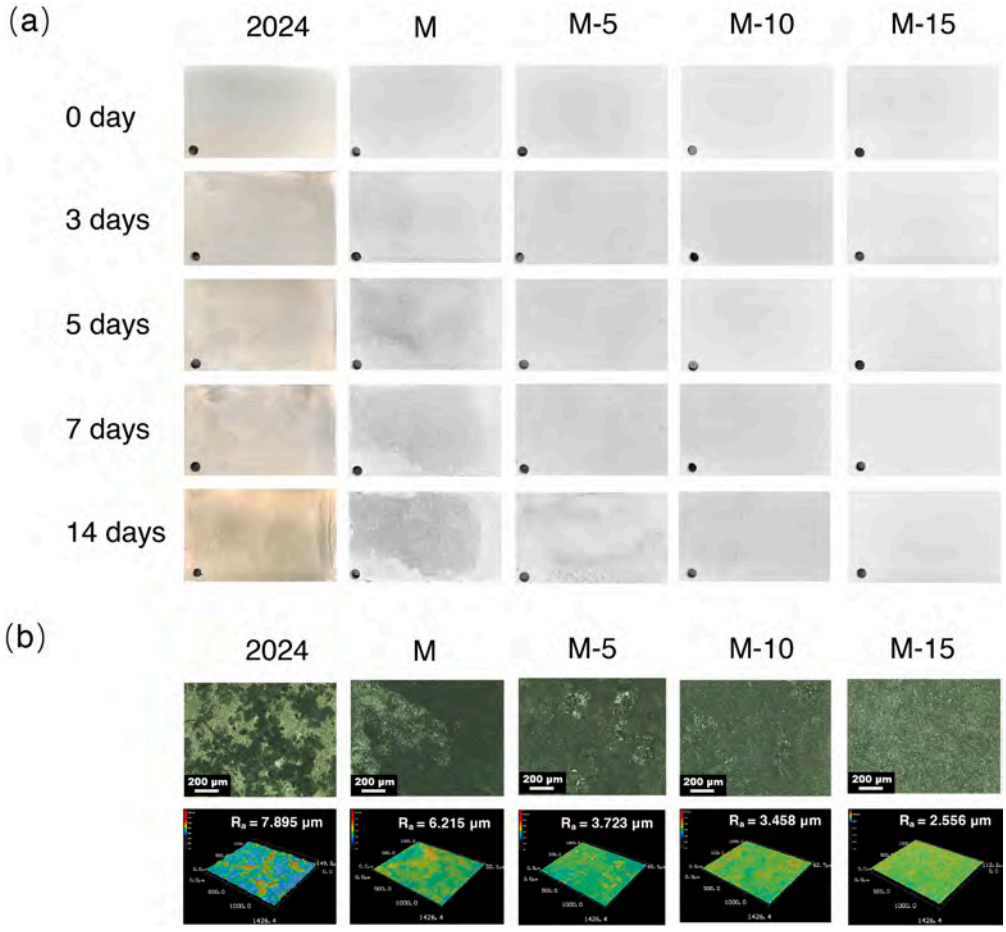

Fig. 8. (a) Digital pictures taken from the 2024 substrate, M, M−5, M−10, and M−15 after immersion for different time; (b) Confocal laser scanning microscopy (CLSM) and 3D topography images after immersion for 14 days of the untreated and MAO 2024 Al samples in 3.5 wt% NaCl.

surface after 14 days. With regard to the samples with sericite, the corrosion damage decreases compared to M. Localized corrosion is much less severe on M−5 than M. Slight corrosion damage starts on the 5th day on M−10 and the corroded area is much smaller than the M−5 sample. After 14 days, the surface on M−15 remains intact and no visible corrosion damage can be observed.

Fig. 8(b) displays the CLSM and 3D topographic images to assess micro-area corrosion after immersion for 14 days. As shown in Fig. 8(b), the 2024 substrate shows an extensively corroded surface that is uneven, cracked, and covered by corrosion products. Corrosion products and crater-like pitting observed from the laser and 3D topographic images of M, M−5, and M−10 decrease after incorporating sericite microplates, which is consistent with the photos above. M−15 shows no apparent local corrosion. The average roughness (R_a) of samples after corrosion reveals that with sericite, the surface morphology is smoother.

Fig. 9 shows the microscopic morphology and EDS results of the sample after immersion in 3.5 wt% NaCl for 14 days. As shown in Fig. 9 (a-b), the surface of M is fully covered by porous and particle-like corrosion products. Moreover, severe intergranular corrosion appears from the substrate under the damaged coating. This may be due to galvanic coupling between the Cu-rich phases (Al_2CuMg and Al_2Cu) and matrix, resulting in the preferential dissolution of the copper-depleted zone along the grain boundaries [4,71]. Corrosion of the substrate leads to grain rupture and the generation of hydrogen and corrosion products, which result in localized fracture in the coatings [70,72]. EDS (Fig. 9c) reveals that the main corrosion products are oxide or hydroxide of aluminum. According to Fig. 9(d) and 9(e), similar cracks and corrosion products appear from M−5 after immersion, but the number and size of the cracks are smaller than that of M, indicating that even a small amount of sericite in the MAO coating can mitigate corrosion. EDS shows that the Al/O concentration ratio of M−5 is smaller than that of M also indicative of less corrosion. Compared with M and M−5, the surface of M−10 is more intact and shows fewer cracks. Although some corrosion products can be observed on M−10, the amount is much less than that on M and M−5. The surface of M−15 is relatively intact without serious fracture and conspicuous corrosion products, indicating that the sericite-incorporated coating has mitigated the corrosion of the substrate. As shown in Fig. 9(j) and 9(k), sericite plates exist around the opening of the micro-pores, thus providing evidence that the sericite plates might seal the micro-pores to block diffusion of the corrosive medium.

In order to analyze the internal state of the coatings after immersion for 2 weeks in 3.5 wt% NaCl, cross-sectional SEM images and EDS maps are obtained. As shown in Fig. 10(a), the surface of M is damaged by corrosion and there are deep cracks between the surface and substrate for passage of the corrosive medium. Fig. 10(b) shows that M−15 has a relatively intact surface after immersion for 14 days and the Si element is distributed in the surface area and pores of the coating, implying that sericite microplates formed a corrosion-resistant barrier in the coating.

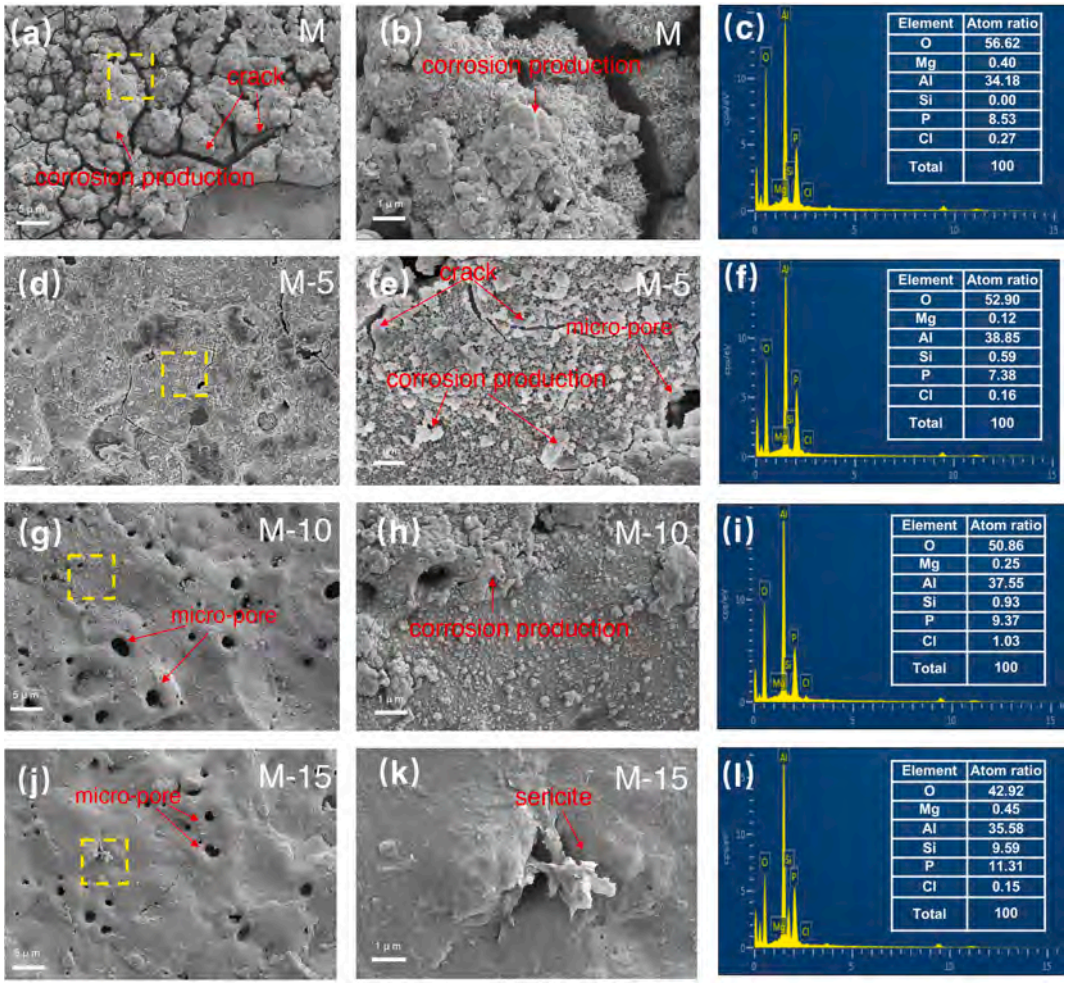

Fig. 9. SEM images of M, M−5, M−10, and M−15 with defects after immersion in 3.5 wt% NaCl of 14 days together with the EDS spectra and elemental concentrations: (a–c) M, (d–f) M−5, (g–i) M−10, and (j–l) M−15.

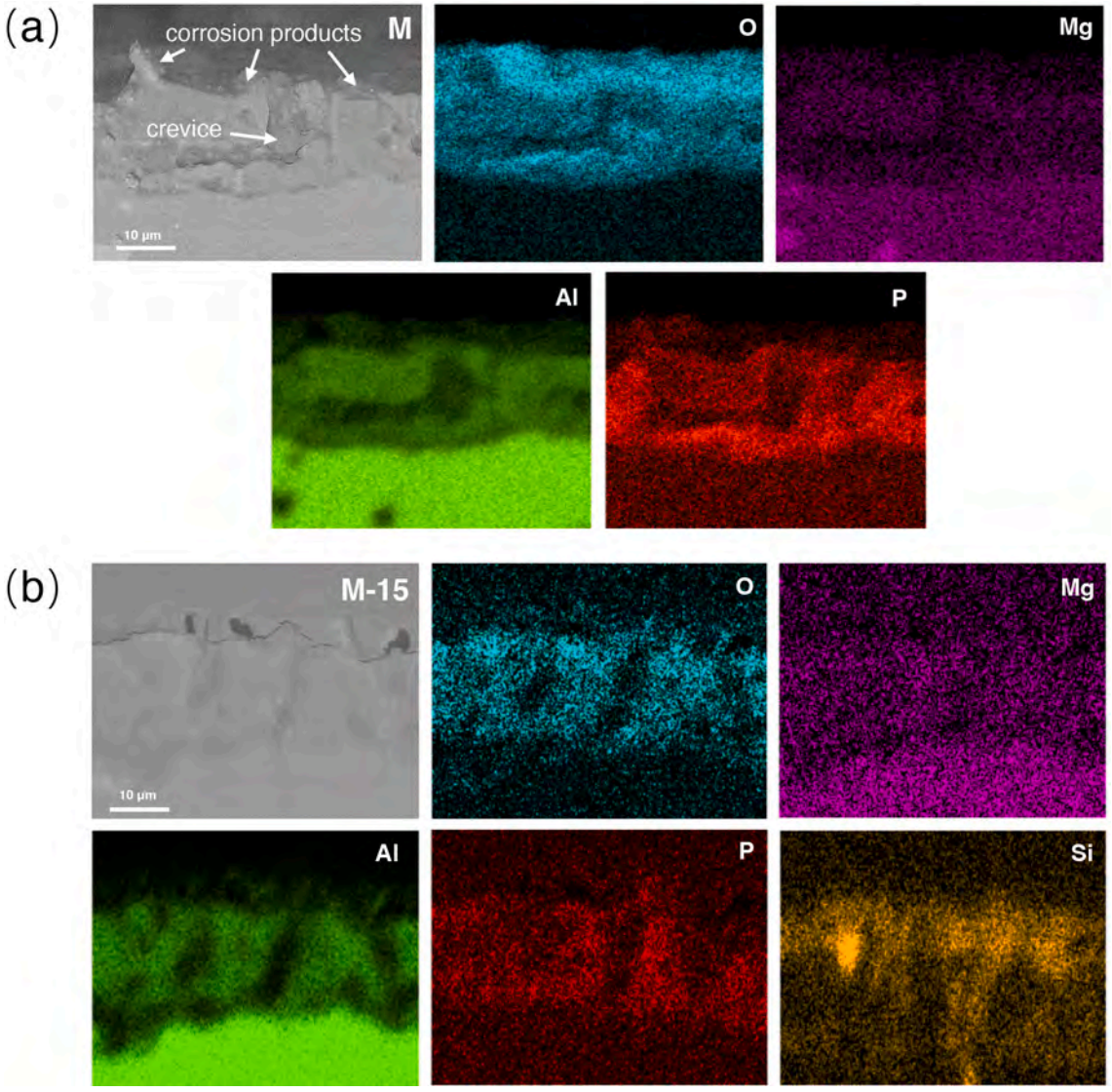

Fig. 10. Cross-sectional SEM images of M and M−15 after immersion in 3.5 wt% NaCl for 14 days and EDS maps of different elements.

3.6. Anti-corrosion mechanism

The main reactions occurring during corrosion of aluminum alloys in NaCl solution are discussed in literatures [35,73–75]. In the course of aluminum corrosion, the anodic activity comes from the dissolution of Al, as shown in (1).

$$Al \rightarrow Al^{3+} + 3e^{-} \quad (1)$$

Simultaneously, the electrons generated are consumed by the cathodic reactions, which can be possibly oxygen reduction reaction (ORR) or hydrogen evolution reaction (HER), as shown in (2) and (3), respectively.

$$O_2 + 2H_2O + 4e^{-} \rightarrow 4OH^{-} \quad (2)$$

$$2H_2O + 2e^{-} \rightarrow H_2 + 2OH^{-} \quad (3)$$

The free Al^{3+} generated from (1) can easily hydrolyze in solution, leading to corrosion product formation and local decrease of pH value, as shown in (4).

$$Al^{3+} + nH_2O \rightarrow Al(OH)_n^{(3-n)} + nH^{+}, \; n = 1, 2, 3 \quad (4)$$

The amorphous corrosion product $Al(OH)_3$ can transform to more stable hydrate oxide, as shown in (5).

$$2Al(OH)_3 \rightarrow Al_2O_3 + 3H_2O \quad (5)$$

Hence, the surfaces of aluminum or aluminum alloys are covered by passivating hydroxide or oxide, which produces corrosion resistance in aqueous solutions, except pitting corrosion in solutions containing halides such as Cl^{-} [76]. In chloride solutions, Cl^{-} can destroy the passivation layer to accelerate corrosion of aluminum by reactions (6).

$$Al(OH)_3 + nCl^{-} \rightarrow Al(OH)_{3-n}Cl_n + nOH^{-}, \; n = 1, 2, 3 \quad (6)$$

It has also been reported that Cl^{-} can permeate and break down the passive oxide film by reacting with aluminum oxide [77–79]. The Cl^{-} ions can also promote the dissolution of Al by coordination, as shown in (7).

$$Al^{3+} + 3Cl^{-} \rightarrow AlCl_3 \quad (7)$$

Therefore, Cl^{-} plays a crucial role in the dissolution of surface oxide and pitting corrosion [77]. The access of H_2O, O_2, and Cl^{-} to the metallic interface is a critical factor affecting corrosion of Al and Al alloys. Furthermore, galvanic effects also have a significant impact on the corrosion resistance of aluminum alloys. Intermetallic particles and alloy elements can form local electrochemical cells with the aluminum

matrix, leading to severe localized attack through pitting in corrosive media.

In the early stage of corrosion of the M sample, the MAO coating consisting of aluminum oxide and $AlPO_4$ retards corrosion to a certain extent. However, as the immersion time increases, the corrosive medium diffuses through the outer layer via micro-pores and defects to reach the inner layer and substrate (Fig. 11a). As aforementioned, Cl^- migrates through the oxide film, causing adsorption and ion displacement on the oxide surface and further inducing undulations at the interface and structural inhomogeneity on the film side [79]. Based on the continuous erosion effect of Cl^-, the inner layer in the MAO coating is broken and corroded, as shown in Fig. 11(b). When the surface of the 2024 substrate is exposed to the corrosive medium, ionization of aluminum and hydrolysis of Al^{3+} take place rapidly [80]. Cl^- migration and Al dissolution lead to the formation of Cl-Al islands and hydrogen production at the oxide/metal interface [81,82]. Therefore, stress buildup occurs by incorporating Cl^- into the oxide film and localized corrosion such as pitting and blister formation beneath the oxide film, finally collapsing the oxide film [83,84]. Hence, as shown in Fig. 9 and Fig. 10, the M sample shows large-area cracking and corrosion products after immersion test, indicating a highly corroded surface.

According to the aforementioned corrosion mechanism and anti-corrosion mechanism of 2D materials in coatings [35,37,38], the anti-corrosion mechanism of sericite microplates in MAO coating is discussed. Cracks and micro-pores in the outer layer of the MAO coating provide pathways for the ingress of corrosive media, leading to caustic corrosion of the substrate. Due to their large aspect ratio and layered structure, the well-dispersed sericite microplates can form a barrier network in MAO coating against the diffusion of corrosive media (Fig. 11c). The penetration of O_2, Cl^- and H_2O is inhibited by the incorporated sericite microplates, thereby suppressing the cathodic corrosion reactions at the coating/substrate interface. As the concentration of sericite in MAO coating increases, the gaps between sericite microplates become smaller and the diffusion pathway of corrosive media becomes more tortuous, which leads to a significant improvement in the corrosion resistance of the coating. Moreover, different from other 2D materials with good conductivity, such as graphene and MXenes, the non-conductivity of sericite can avoid the risk of causing galvanic corrosion with the aluminum alloy substrate. The incorporation of sericite microplates can reduce the ingress of corrosive media without causing galvanic corrosion, thereby improving the long-term corrosion resistance of the MAO coating.

3.7. Tribological tests and anti-wear mechanism

The tribological experiments are performed with GCr15 steel balls as the counterpart at a load of 2 N. Fig. 12(a) depicts the change in the friction coefficients of the 2024 aluminum alloy and MAO coatings under dry friction conditions. The friction coefficient of the bare 2024 Al substrate is between 0.3 and 0.5 and fluctuates wildly. The MAO coatings show relatively stable COFs, which are further reduced by incorporating sericite microplates. The COF of M is about 0.6, which is the largest of all MAO samples. In contrast, the COF of M−5 is reduced to ~ 0.5. The average stable COFs of M−10 and M−15 are 0.3 and 0.25, respectively, smaller than those of M and M−5. The results show that after the sericite concentration in MAO coating reaches a certain value, the COF value exhibits a significant decrease, indicating that the sericite microplates have an excellent lubricating effect in friction.

Fig. 12(b) and (c) show the 2D profiles and 3D morphology of the wear tracks on the 2024 aluminum alloy and MAO coatings. The 2024 Al alloy shows severe wear as manifested by deep scratch and small debris on the wear track. In contrast, the wear tracks on the MAO coatings are smoother and more indistinct, indicating the suppression of adhesive wear. For MAO samples, the width and depth of wear tracks decrease

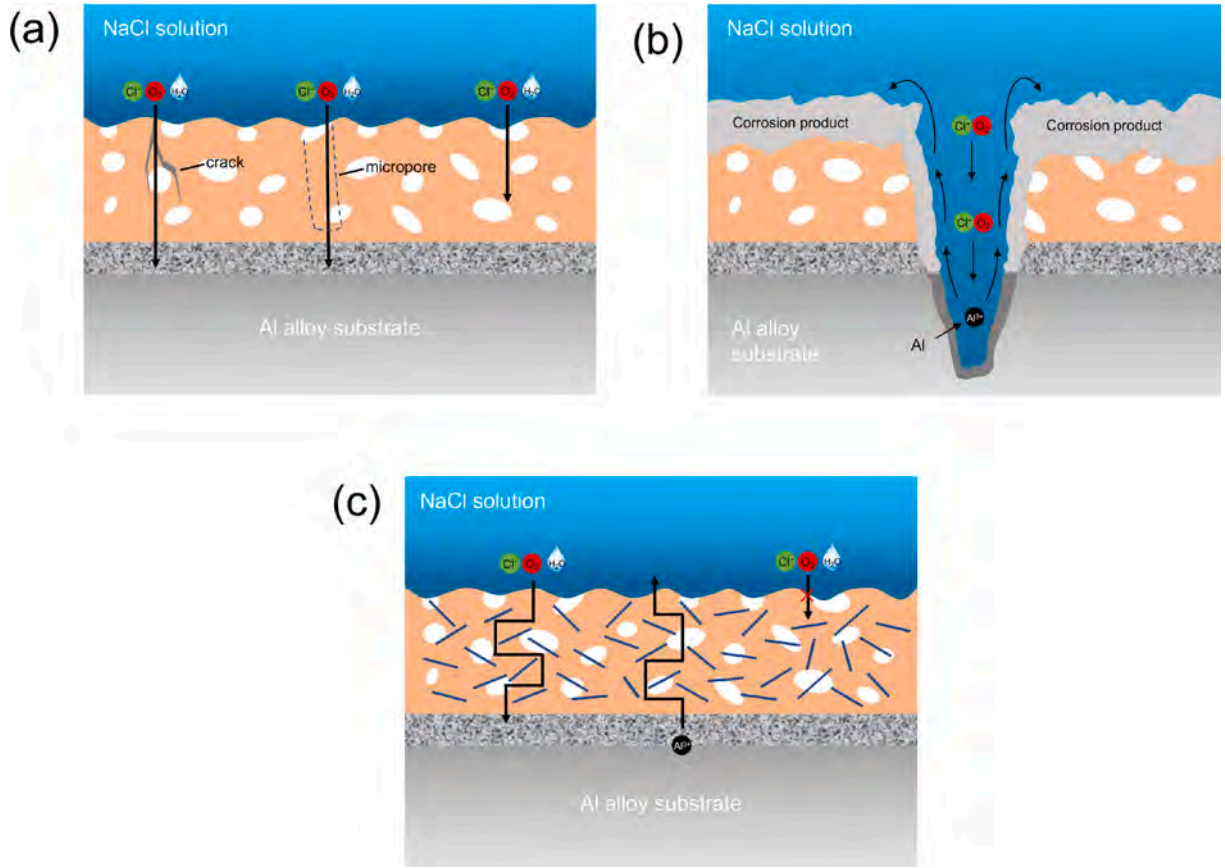

Fig. 11. Schematics illustrating the corrosion mechanism of the MAO coatings (a, b) without and (c) with sericite incorporation.

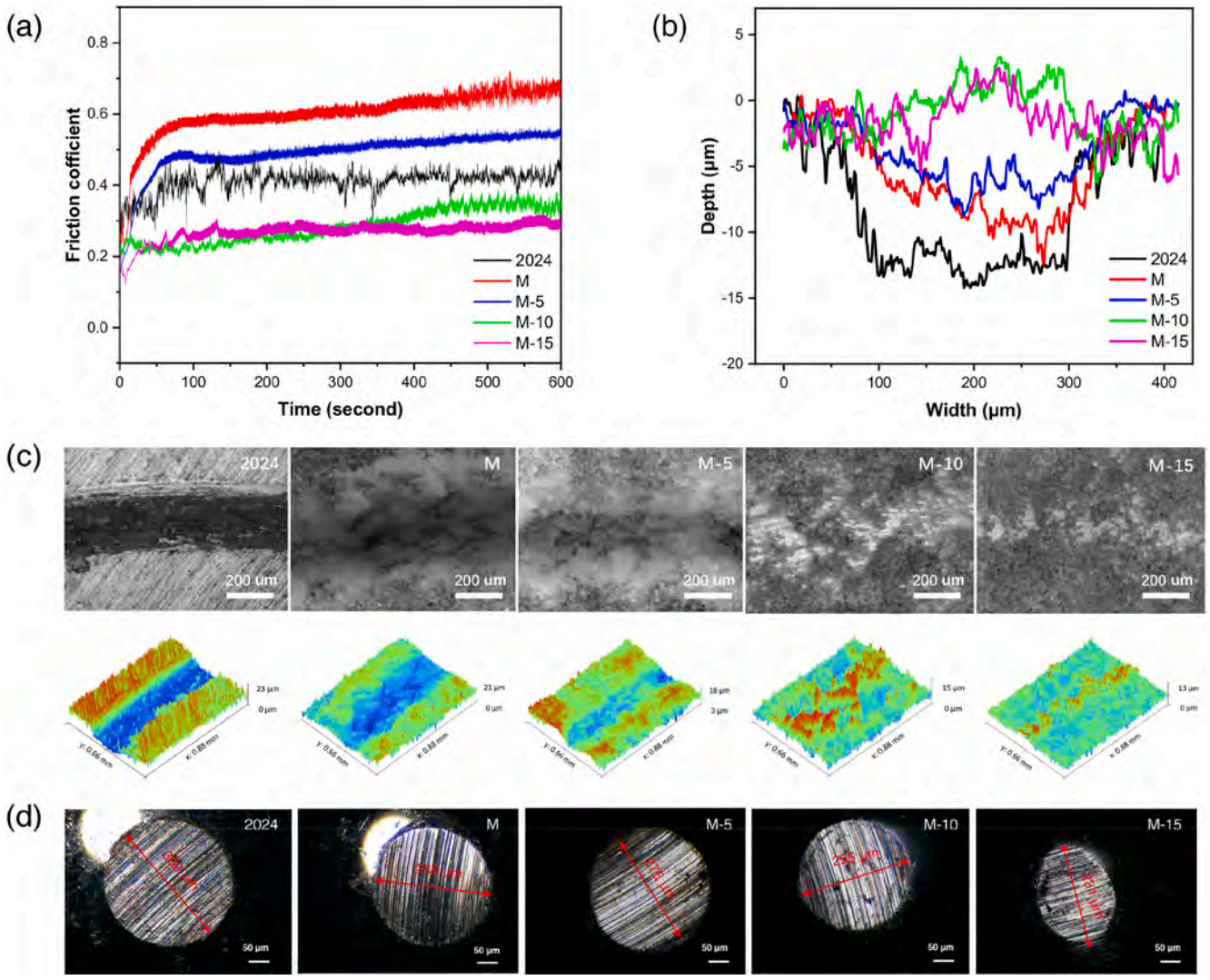

Fig. 12. (a) Friction coefficients as a function of time; (b) 2D profile; (c) Confocal laser scanning images and 3D morphologies of the worn surfaces on the 2024 substrate, M, M−5, M−10, and M−15; (d) The wear scars of counterpart balls for 2024 substrate, M, M−5, M−10, and M−15 samples.

with sericite addition. Among them, both the M−10 and M−15 samples show almost no wear loss of the coating, and the M−15 sample has the narrowest wear track. Fig. 12(d) shows the wear scars of the ball counterface. The diameters of the wear scars against samples decrease from 309 μm to 231 μm following the order from 2024 Al to M−15. These diameters can approximately correspond to the wear rate of the steel ball [33]. Therefore, for the M−15 sample, it can be seen that the wear of sample and counterpart is simultaneously alleviated, and the friction coefficient is significantly reduced, suggesting improved anti-wear performance.

To study the anti-wear mechanism of the MAO coatings with and without sericite microplates, SEM and EDS are employed to characterize the worn area of M and M−15. As shown in Fig. 13(a–b), worn track on M exhibits a rough and delaminated morphology, indicating a plasticity-dominated wear behavior. Micro-cracks are also observed from the groove of wear track on the M sample, which is the characteristic of mechanical degradation via fatigue wear mechanism [85]. The EDS results of Al and Fe indicate that debris and particles fall off from the GCr15 counterpart under stress during friction, which further worsens the wear and decreases the anti-wear performance of the coatings [86,87]. Compared to M, M−15 shows a narrower wear track with a predominantly polished surface and flat sheet-like regions, indicating the existence of the tribo-transfer film (Fig. 13 c-d). The EDS result in Fig. 13(c) shows that the transfer film region has a high concentration of Fe, which can be due to the adhesive wear debris of steel ball generated during the wear process. It is noted that the magnified area of the tribo-transfer film shows a higher concentration of Si (4.26%) than M−15 without friction, as shown in Fig. 13(c), suggesting that the sericite microplates also take place in the formation of the tribo-transfer film.

According to the above results, the related mechanism is discussed. With regard to the M sample, as shown in Fig. 14(a), the outer layer is partly delaminated by the friction pair under the pressure and shear stress to form distinct grooves. The exfoliated debris and the contact area increase during the counterpart movement, leading to a higher friction coefficient and more serious wear [88]. Meanwhile, the steel ball counterpart is also peeled off by the MAO coating, leaving traces of Fe on the wear tracks. The M−15 sample contains the highest concentration of sericite, which possess good self-lubricating property and has been used as solid lubricants [89,90]. The slip of the (0 0 2) lattice planes and dissociation of the Si-O layer structure provide lubricating effects during wear. Moreover, as a quasi-2D material, the sericite microplate with a large specific surface area can facilitate the formation of the tribo-transfer film (Fig. 14b). At the beginning of the friction process of M−15, due to the improved hardness of MAO coating, the counterpart ball is relatively more like to be worn by the coating surface at the micro level [91,92]. Then the wear debris generated by friction adheres to the wear

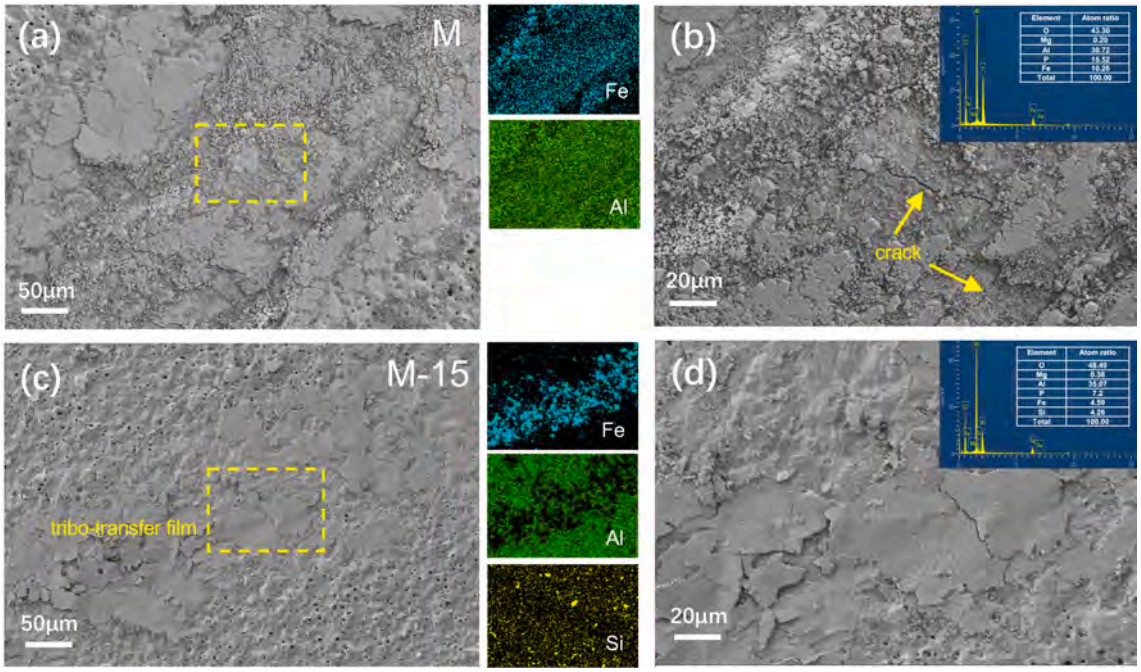

Fig. 13. SEM images of the worn surfaces: (a-b) M and (c-d) M−15 MAO coatings on Al under a load of 2 N under dry friction conditions. The insets show the EDS maps and spectra of the indicated areas.

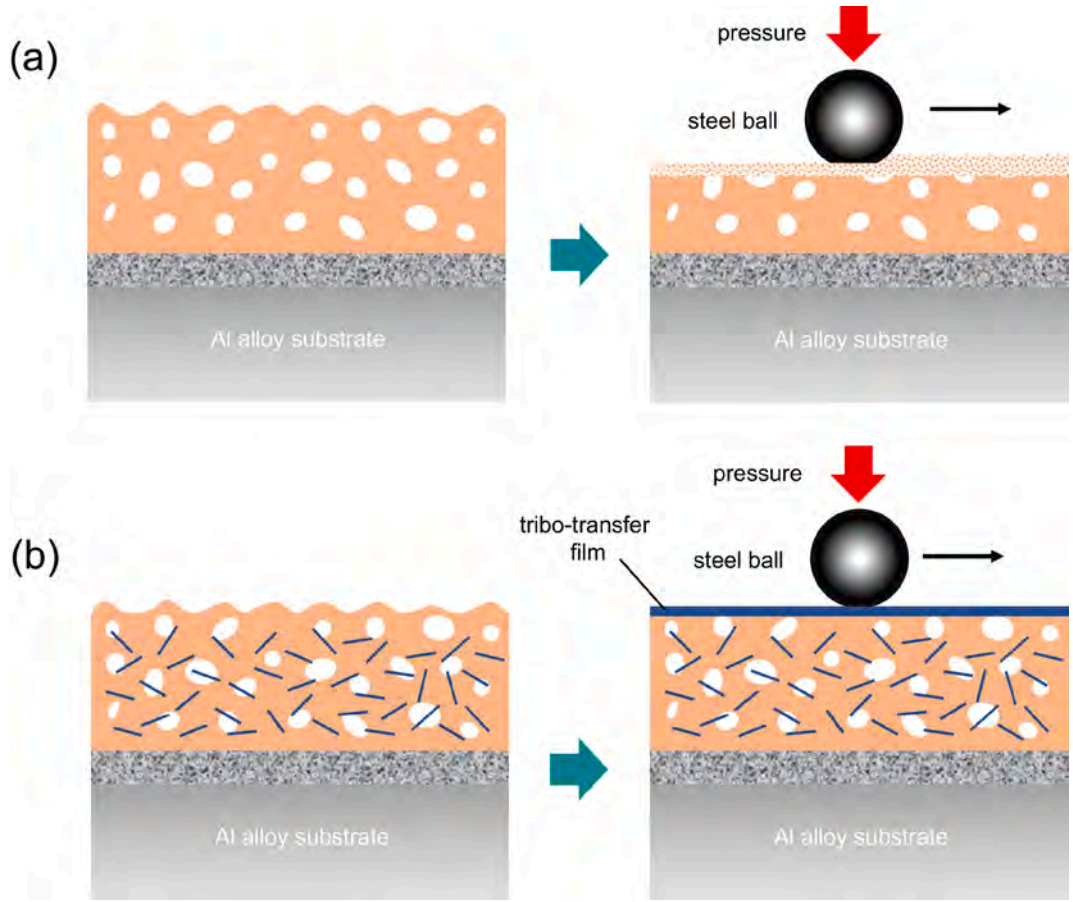

Fig. 14. Schematics illustrating the wear mechanism of the MAO coatings (a) without and (b) with sericite incorporation.

track and forms a surface transfer film under the synergetic effect of frictional heat and pressure [93]. The tribo-transfer film can reduce the contact between the counterpart steel balls and MAO coatings, thereby alleviating the adhesive friction and bringing the friction process into a stable stage [33,88].

4. Conclusion

In this work, quasi-2D sericite microplates are prepared from natural sericite and added into the MAO electrolyte of 2024 Al alloy. The characterization results indicate that sericite microplates are successfully incorporated into the MAO coating. The anti-corrosion and anti-wear properties of the MAO coatings improve with the addition of sericite microplates. The M−15 sample exhibited the highest corrosion resistance and the lowest wear rate and COF. The enhanced corrosion resistance stems from the barrier effects of sericite microplates reducing the intrusion of the corrosive media, and the improved wear performance is mainly due to the formation of the tribo-transfer film. Our findings provide new and valuable information for the design and fabrication of future anti-corrosion/wear MAO coatings to expand the industrial applications of Al alloys.

CRediT authorship contribution statement

Ke Xi: Investigation, Writing – original draft, Data curation, Visualization. **Hao Wu:** Conceptualization, Methodology, Formal analysis, Investigation, Writing – review & editing, Visualization, Funding acquisition, Project administration. **Chilou Zhou:** Validation, Funding acquisition. **Ziyang Qi:** Investigation. **Kailong Yang:** Investigation. **Ricky K.Y. Fu:** Resources. **Shu Xiao:** Investigation. **Guosong Wu:** Investigation. **Kejian Ding:** Resources. **Guohua Chen:** Supervision. **Paul K. Chu:** Writing – review & editing, Funding acquisition.

Declaration of Competing Interest

The authors declare that they have no known competing financial interests or personal relationships that could have appeared to influence the work reported in this paper.

Acknowledgements

The work was financially supported by the National Natural Science Foundation of China (Nos. 51905177 and 52075183), China Postdoctoral Science Foundation (Nos. 2019M662899 and 2019M662909), Fundamental Research Funds for the Central Universities (No. 2019MS061), Guangdong Basic and Applied Basic Research Foundation (No. 2019A1515011157), as well as City University of Hong Kong Strategic Research Grant (No. 7005505). We thank Prof. Fenghua Su and Mr. Xin Xu for providing help and instrument for tribological experiments.

Appendix A. Supplementary material

Supplementary data to this article can be found online at https://doi.org/10.1016/j.apsusc.2022.152693.

References

[1] S. Chu, A. Majumdar, Opportunities and challenges for a sustainable energy future, Nature 488 (2012) 294–303.
[2] M. Sokoluk, C. Cao, S. Pan, X. Li, Nanoparticle-enabled phase control for arc welding of unweldable aluminum alloy 7075, Nat. Commun. 10 (2019) 98.
[3] F. Shamsi, M. Khorasanian, S.M. Lari Baghal, Effect of potassium permanganate on corrosion and wear properties of ceramic coatings manufactured on CP-aluminum by plasma electrolytic oxidation, Surf. Coat. Technol. 346 (2018) 63–72.
[4] V. Guillaumin, G. Mankowski, Localized corrosion of 2024 T351 aluminium alloy in chloride media, Corros. Sci. 41 (3) (1998) 421–438.
[5] R.S. Long, E. Boettcher, D. Crawford, Current and Future Uses of Aluminum in the Automotive Industry, JOM 69 (2017) 2635–2639.
[6] L. Wen, Y. Wang, Y. Zhou, J.H. Ouyang, L. Guo, D. Jia, Corrosion evaluation of microarc oxidation coatings formed on 2024 aluminium alloy, Corros. Sci. 52 (8) (2010) 2687–2696.
[7] D. Mehta, S. Masood, W. Song, Investigation of wear properties of magnesium and aluminum alloys for automotive applications, J. Mater. Process. Technol. 155 (2004) 1526–1531.
[8] S.A. Abdel-Gawad, W.M. Osman, A.M. Fekry, Characterization and corrosion behavior of anodized aluminum alloys for military industries applications in artificial seawater, Surf. Interfaces 14 (2019) 314–323.
[9] M.I. Bashir, M. Shafiq, M. Naeem, M. Zaka-ul-Islam, J.C. Díaz-Guillén, C.M. Lopez-Badillo, M. Zakaullah, Enhanced surface properties of aluminum by PVD-TiN coating combined with cathodic cage plasma nitriding, Surf. Coat. Technol. 327 (2017) 59–65.
[10] C. Lu, J.W. Yao, Y.X. Wang, Y.D. Zhu, J.H. Guo, Y. Wang, H.Y. Fu, Z.B. Chen, M. F. Yan, A novel anti-frictional multiphase layer produced by plasma nitriding of PVD titanium coated ZL205A aluminum alloy, Appl. Surf. Sci. 431 (2018) 32–38.
[11] L. Yin, Y. Jin, C. Leygraf, J. Pan, A FEM model for investigation of micro-galvanic corrosion of Al alloys and effects of deposition of corrosion products, Electrochimica Acta 192 (2016) 310–318.
[12] M. Yu, H. Dong, H. Shi, L. Xiong, C. He, J. Liu, S. Li, Effects of graphene oxide-filled sol-gel sealing on the corrosion resistance and paint adhesion of anodized aluminum, Appl. Surf. Sci. 479 (2019) 105–113.
[13] M. Terada, F.M. Queiroz, D.B.S. Aguiar, V.H. Ayusso, H. Costenaro, M.G. Olivier, H.G. de Melo, I. Costa, Corrosion resistance of tartaric-sulfuric acid anodized AA2024-T3 sealed with Ce and protected with hybrid sol–gel coating, Surf. Coat. Technol. 372 (2019) 422–426.
[14] D. Ravnikar, N.B. Dahotre, J. Grum, Laser coating of aluminum alloy EN AW 6082–T651 with TiB2 and TiC: microstructure and mechanical properties, Appl. Surf. Sci. 282 (2013) 914–922.
[15] T.M. Yue, L.J. Yan, C.P. Chan, C.F. Dong, H.C. Man, G.K.H. Pang, Excimer laser surface treatment of aluminum alloy AA7075 to improve corrosion resistance, Surf. Coat. Technol. 179 (2004) 158–164.
[16] G. da Silva Savonov, M.G.G. Camarinha, L.O. Rocha, M.J.R. Barboza, G.V. Martins, D.A.P. Reis, Study of the influence of the RRA thermal treatment and plasma nitriding on corrosion behavior of 7075–T6 aluminum alloy, Surf. Coat. Technol. 374 (2019) 736–744.
[17] A. Yerokhin, X. Nie, A. Leyland, A. Matthews, S. Dowey, Plasma electrolysis for surface engineering, Surf. Coat. Technol. 122 (1999) 73–93.
[18] S. Moon, Y. Jeong, Generation mechanism of microdischarges during plasma electrolytic oxidation of Al in aqueous solutions, Corros. Sci. 51 (2009) 1506–1512.
[19] Q. Li, J. Liang, B. Liu, Z. Peng, Q. Wang, Effects of cathodic voltages on structure and wear resistance of plasma electrolytic oxidation coatings formed on aluminium alloy, Appl. Surf. Sci. 297 (2014) 176–181.
[20] J. Zhao, X. Xie, C. Zhang, Effect of the graphene oxide additive on the corrosion resistance of the plasma electrolytic oxidation coating of the AZ31 magnesium alloy, Corros. Sci. 114 (2017) 146–155.
[21] X.-J. Li, M. Zhang, S. Wen, X. Mao, W.-G. Huo, Y.-Y. Guo, Y.-X. Wang, Microstructure and wear resistance of micro-arc oxidation ceramic coatings prepared on 2A50 aluminum alloys, Surf. Coat. Technol. 394 (2020) 125853, https://doi.org/10.1016/j.surfcoat.2020.125853.
[22] X. Lu, M. Mohedano, C. Blawert, E. Matykina, R. Arrabal, K.U. Kainer, M. L. Zheludkevich, Plasma electrolytic oxidation coatings with particle additions – A review, Surf. Coat. Technol. 307 (2016) 1165–1182.
[23] M. Mu, J. Liang, X. Zhou, Q. Xiao, One-step preparation of TiO2/MoS2 composite coating on Ti6Al4V alloy by plasma electrolytic oxidation and its tribological properties, Surf. Coat. Technol. 214 (2013) 124–130.
[24] J. Liang, P.B. Srinivasan, C. Blawert, W. Dietzel, Influence of pH on the deterioration of plasma electrolytic oxidation coated AM50 magnesium alloy in NaCl solutions, Corros. Sci. 52 (2010) 540–547.
[25] A. Mandelli, M. Bestetti, A. Da Forno, N. Lecis, S.P. Trasatti, M. Trueba, A composite coating for corrosion protection of AM60B magnesium alloy, Surf. Coat. Technol. 205 (2011) 4459–4465.
[26] A. Bahramian, K. Raeissi, A. Hakimizad, An investigation of the characteristics of Al2O3/TiO2 PEO nanocomposite coating, Appl. Surf. Sci. 351 (2015) 13–26.
[27] M. Kaseem, Y.H. Lee, Y.G. Ko, Incorporation of MoO 2 and ZrO 2 particles into the oxide film formed on 7075 Al alloy via micro-arc oxidation, Mater. Lett. 182 (2016) 260–263.
[28] S. Fatimah, M.P. Kamil, J.H. Kwon, M. Kaseem, Y.G. Ko, Dual incorporation of SiO 2 and ZrO 2 nanoparticles into the oxide layer on 6061 Al alloy via plasma electrolytic oxidation: Coating structure and corrosion properties, J. Alloy. Compd. 707 (2017) 358–364.
[29] M. Kaseem, Y.G. Ko, A novel composite system composed of zirconia and LDHs film grown on plasma electrolysis coating: Toward a stable smart coating, Ultrason Sonochem 49 (2018) 316–324.
[30] M. Kaseem, J.H. Min, Y.G. Ko, Corrosion behavior of Al-1wt% Mg-0.85wt%Si alloy coated by micro-arc-oxidation using TiO2 and Na2MoO4 additives: role of current density, J. Alloy. Compd. 723 (2017) 448–455.
[31] Q. Huang, Z. Wu, H. Wu, S. Ji, Z. Ma, Z. Wu, P. Chen, J. Zhu, R.K.Y. Fu, H. Lin, X. Tian, F. Pan, P.K. Chu, Corrosion behavior of ZnO-reinforced coating on aluminum alloy prepared by plasma electrolytic oxidation, Surf. Coat. Technol. 374 (2019) 1015–1023.
[32] A. Pardo, S. Merino, M.C. Merino, I. Barroso, M. Mohedano, R. Arrabal, F. Viejo, Corrosion behaviour of silicon–carbide-particle reinforced AZ92 magnesium alloy, Corros. Sci. 51 (2009) 841–849.

[33] H. Yan, L. Zhang, H. Li, X. Fan, M. Zhu, Towards high-performance additive of Ti3C2/graphene hybrid with a novel wrapping structure in epoxy coating, Carbon 157 (2020) 217–233.

[34] J. Ding, H. Zhao, Z. Shao, H. Yu, Bioinspired Smart Anticorrosive Coatings with an Emergency-Response Closing Function, ACS Appl Mater Interfaces 11 (2019) 42646–42653.

[35] H. Yan, J. Wang, C. Meng, X. Wang, S. Song, X. Fan, L. Zhang, H. Li, W. Li, M. Zhu, Towards long-term corrosion and wear protection of Al alloy: synergy of Ti3C2Tx flake and micro-arc oxidation coating, Corros. Sci. 174 (2020).

[36] X. Zhu, Q. Yan, L.i. Cheng, H. Wu, H. Zhao, L. Wang, Self-alignment of cationic graphene oxide nanosheets for anticorrosive reinforcement of epoxy coatings, Chem. Eng. J. 389 (2020) 124435, https://doi.org/10.1016/j.cej.2020.124435.

[37] Y. Zhang, J. Tian, J. Zhong, X. Shi, Thin Nacre-Biomimetic Coating with Super-Anticorrosion Performance, ACS Nano 12 (2018) 10189–10200.

[38] Z.-Y. Li, Z.-B. Cai, Y. Ding, X.-J. Cui, Z.-b. Yang, M.-H. Zhu, Characterization of graphene oxide/ZrO2 composite coatings deposited on zirconium alloy by micro-arc oxidation, Appl. Surf. Sci. 506 (2020) 144928, https://doi.org/10.1016/j.apsusc.2019.144928.

[39] R. Askarnia, S.R. Fardi, M. Sobhani, H. Staji, H. Aghamohammadi, Effect of graphene oxide on properties of AZ91 magnesium alloys coating developed by micro-arc oxidation process, J. Alloy. Compd. 892 (2022) 162106, https://doi.org/10.1016/j.jallcom.2021.162106.

[40] C. Cui, A.T.O. Lim, J. Huang, A cautionary note on graphene anti-corrosion coatings, Nat. Nanotechnol. 12 (2017) 834–835.

[41] M. Schriver, W. Regan, W.J. Gannett, A.M. Zaniewski, M.F. Crommie, A. Zettl, Graphene as a Long-Term Metal Oxidation Barrier: worse Than Nothing, ACS Nano 7 (7) (2013) 5763–5768.

[42] Y. Shih, Y. Shen, Swelling of sericite by LiNO3-hydrothermal treatment, Appl. Clay Sci. 43 (2009) 282–288.

[43] H. Ding, X. Xu, N. Liang, Y.B. Wang, Preparation sericite nanoflakes by exfoliation of wet ultrafine grinding, in, Advanced Materials Research, Trans Tech Publ 178 (2011) 242–247.

[44] Y. Liang, W. Jiang, H. Ding, Y. Wang, The modification and characterization of thermal-treated sericite by fluorosilicate, Sci. Rep. 8 (2018) 14293.

[45] N.H. Abdullah, K. Shameli, E.C. Abdullah, L.C. Abdullah, Low cost and efficient synthesis of magnetic iron oxide/activated sericite nanocomposites for rapid removal of methylene blue and crystal violet dyes, Mater. Charact. 163 (2020), 110275.

[46] Lalhmunsiama, D. Tiwari, S.-M. Lee, Physico-chemical studies in the removal of Sr (II) from aqueous solutions using activated sericite, J. Environ. Radioact. 147 (2015) 76–84.

[47] H. Ding, Y. Wang, Y.u. Liang, F. Qin, Preparation and Characterization of Cetyl Trimethylammonium Intercalated Sericite, Adv. Mater. Sci. Eng. 2014 (2014) 1–8.

[48] B. Paul, W.N. Martens, R.L. Frost, Organosilane grafted acid-activated beidellite clay for the removal of non-ionic alachlor and anionic imazaquin, Appl. Surf. Sci. 257 (13) (2011) 5552–5558.

[49] Lalhmunsiama, D. Tiwari, S.-M. Lee, Lee, Physico-chemical studies in the removal of Sr(II) from aqueous solutions using activated sericite, J. Environ. Radioact. 147 (2015) 76–84.

[50] M. von Smoluchowski, Contribution à la théorie de l'endosmose électrique et de quelques phénomènes corrélatifs, Bull. Akad. Sci. Cracovie. 8 (1903) 182–200.

[51] V. Dehnavi, D.W. Shoesmith, B.L. Luan, M. Yari, X.Y. Liu, S. Rohani, Corrosion properties of plasma electrolytic oxidation coatings on an aluminium alloy–The effect of the PEO process stage, Mater. Chem. Phys. 161 (2015) 49–58.

[52] C. Blawert, S. Karpushenkov, M. Serdechnova, L. Karpushenkava, M. Zheludkevich, Plasma electrolytic oxidation of zinc alloy in a phosphate-aluminate electrolyte, Appl. Surf. Sci. 505 (2020), 144552.

[53] S. Ignjatović, C. Blawert, M. Serdechnova, S. Karpushenkov, M. Damjanović, P. Karlova, D.C.F. Wieland, M. Starykevich, S. Stojanović, L.j. Damjanović-Vasilić, M.L. Zheludkevich, Formation of multi-functional TiO2 surfaces on AA2024 alloy using plasma electrolytic oxidation, Appl. Surf. Sci. 544 (2021) 148875, https://doi.org/10.1016/j.apsusc.2020.148875.

[54] R.O. Hussein, X. Nie, D.O. Northwood, A. Yerokhin, A. Matthews, Spectroscopic study of electrolytic plasma and discharging behaviour during the plasma electrolytic oxidation (PEO) process, J. Phys. D Appl. Phys. 43 (10) (2010) 105203, https://doi.org/10.1088/0022-3727/43/10/105203.

[55] R.O. Hussein, X. Nie, D.O. Northwood, An investigation of ceramic coating growth mechanisms in plasma electrolytic oxidation (PEO) processing, Electrochimica Acta 112 (2013) 111–119.

[56] L. Zhu, X. Ke, J. Li, Y. Zhang, Z. Zhang, M. Sui, Growth mechanisms for initial stages of plasma electrolytic oxidation coating on Al, Surf. Interfaces 25 (2021) 101186, https://doi.org/10.1016/j.surfin.2021.101186.

[57] S. Ji, Y. Weng, Z. Wu, Z. Ma, X. Tian, R.K.Y. Fu, H. Lin, G. Wu, P.K. Chu, F. Pan, Excellent corrosion resistance of P and Fe modified micro-arc oxidation coating on Al alloy, J. Alloy. Compd. 710 (2017) 452–459.

[58] A.K. Sharma, R.U. Rani, A. Malek, K.S.N. Acharya, M. Muddu, S. Kumar, Black anodizing of a magnesium-lithium alloy, Met. Finish. 94 (4) (1996) 16–27.

[59] X. Wu, P. Su, Z. Jiang, S. Meng, Influences of current density on tribological characteristics of ceramic coatings on ZK60 Mg alloy by plasma electrolytic oxidation, ACS Appl Mater Interfaces 2 (3) (2010) 808–812.

[60] H. Wu, G. Wu, P.K. Chu, Effects of cerium ion implantation on the corrosion behavior of magnesium in different biological media, Surf. Coat. Technol. 306 (2016) 6–10.

[61] X. Huang, L. Yu, Y. Dong, Corrosion resistance of a novel ceria doped aluminum phosphate ceramic coating on cast Al-Si alloy by steam-assisted curing, Corros. Sci. 182 (2021), 109256.

[62] L. Wen, Y. Wang, Y. Zhou, L. Guo, J.H. Ouyang, Microstructure and corrosion resistance of modified 2024 Al alloy using surface mechanical attrition treatment combined with microarc oxidation process, Corros. Sci. 53 (1) (2011) 473–480.

[63] X.-J. Cui, X.-Z. Lin, C.-H. Liu, R.-S. Yang, X.-W. Zheng, M. Gong, Fabrication and corrosion resistance of a hydrophobic micro-arc oxidation coating on AZ31 Mg alloy, Corros. Sci. 90 (2015) 402–412.

[64] P. Zoltowski, On the electrical capacitance of interfaces exhibiting constant phase element behaviour, J. Electroanal. Chem. 443 (1998) 149–154.

[65] H. Wu, A.M. Qasim, S. Xiao, Q. Huang, F. Zhang, Z. Wu, R.K.Y. Fu, G. Wu, P.K. Chu, Magnetron-sputtered fluorocarbon polymeric film on magnesium for corrosion protection, Surf. Coat. Technol. 352 (2018) 437–444.

[66] G. Wu, X. Zhang, Y. Zhao, J.M. Ibrahim, G. Yuan, P.K. Chu, Plasma modified Mg–Nd–Zn–Zr alloy with enhanced surface corrosion resistance, Corros. Sci. 78 (2014) 121–129.

[67] Y. Zhang, C. Yan, F. Wang, W. Li, Electrochemical behavior of anodized Mg alloy AZ91D in chloride containing aqueous solution, Corros. Sci. 47 (2005) 2816–2831.

[68] Y. Xin, T. Hu, P.K. Chu, Degradation behaviour of pure magnesium in simulated body fluids with different concentrations of HCO3, Corros. Sci. 53 (2011) 1522–1528.

[69] B. Xu, J. Sun, J. Han, Z. Yang, H. Zhou, L. Xiao, S. Xu, Y. Han, A. Ma, G. Wu, Effect of hierarchical precipitates on corrosion behavior of fine-grain magnesium-gadolinium-silver alloy, Corros. Sci. 194 (2022), 109924.

[70] H. Wu, Z. Shi, X. Zhang, A.M. Qasim, S. Xiao, F. Zhang, Z. Wu, G. Wu, K. Ding, P. K. Chu, Achieving an acid resistant surface on magnesium alloy via bio-inspired design, Appl. Surf. Sci. 478 (2019) 150–161.

[71] M.L. de Bonfils-Lahovary, L. Laffont, C. Blanc, Characterization of intergranular corrosion defects in a 2024 T351 aluminium alloy, Corros. Sci. 119 (2017) 60–67.

[72] H. Wang, T. Sun, L. Chang, F. Liu, B. Liu, C. Zhao, X. Xue, X. Xiong, Preparation of Ca doping ZrO 2 coating on NiTi shape memory alloy by cathodic plasma electrolytic deposition and its structure, in-vitro bioactivity and biocompatibility analysis, Surf. Coat. Technol. 325 (2017) 136–144.

[73] R.T. Foley, T.H. Nguyen, The Chemical Nature of Aluminum Corrosion: V. Energy Transfer in Aluminum Dissolution, J. Electrochem. Soc. 129 (1982) 464–467.

[74] O. Guseva, P. Schmutz, T. Suter, O. von Trzebiatowski, Modelling of anodic dissolution of pure aluminium in sodium chloride, Electrochimica Acta 54 (2009) 4514–4524.

[75] H. Ding, L. Hihara, Localized Corrosion Currents and pH Profile over B4C, SiC, and Al2O3 Reinforced 6092 Aluminum Composites: I. In Solution, J. Electrochem. Soc. 152 (2005) B161.

[76] Z. Szklarska-Smialowska, Pitting corrosion of aluminum, Corros. Sci. 41 (1999) 1743–1767.

[77] B. Zaid, D. Saidi, A. Benzaid, S. Hadji, Effects of pH and chloride concentration on pitting corrosion of AA6061 aluminum alloy, Corros. Sci. 50 (2008) 1841–1847.

[78] W.E. O'Grady, D.F. Roeper, P.M. Natishan, Structure of Chlorine K-Edge XANES Spectra During the Breakdown of Passive Oxide Films on Aluminum, The Journal of Physical Chemistry C 115 (2011) 25298–25303.

[79] B. Zhang, J. Wang, B. Wu, X.W. Guo, Y.J. Wang, D. Chen, Y.C. Zhang, K. Du, E. E. Oguzie, X.L. Ma, Unmasking chloride attack on the passive film of metals, Nat. Commun. 9 (2018) 2559.

[80] T. Hagyard, J.R. Williams, Potential of aluminium in aqueous chloride solutions. Part 1, Trans. Faraday Soc. 57 (1961) 2288–2294.

[81] G.T. Burstein, R.M. Souto, Observations of localised instability of passive titanium in chloride solution, Electrochimica Acta 40 (12) (1995) 1881–1888.

[82] E. McCafferty, Sequence of steps in the pitting of aluminum by chloride ions, Corros. Sci. 45 (7) (2003) 1421–1438.

[83] K. Shimizu, G.M. Brown, K. Kobayashi, P. Skeldon, G.E. Thompson, G.C. Wood, A novel approach for the study of the migration of Cl− ions in anodic alumina, Corros. Sci. 41 (9) (1999) 1835–1847.

[84] T.P. Hoar, The production and breakdown of the passivity of metals, Corros. Sci. 7 (6) (1967) 341–355.

[85] F. Muhaffel, M. Kaba, G. Cempura, B. Derin, A. Kruk, E. Atar, H. Cimenoglu, Influence of alumina and zirconia incorporations on the structure and wear resistance of titania-based MAO coatings, Surf. Coat. Technol. 377 (2019) 124900, https://doi.org/10.1016/j.surfcoat.2019.124900.

[86] Z. Zhou, Q. Shan, Y. Jiang, Z. Li, Z. Zhang, Effect of nanoscale V2C precipitates on the three-body abrasive wear behavior of high-Mn austenitic steel, Wear 436 (2019), 203009.

[87] M.-X. Shen, F. Dong, Z.-X. Zhang, X.-K. Meng, X.-D. Peng, Effect of abrasive size on friction and wear characteristics of nitrile butadiene rubber (NBR) in two-body abrasion, Tribol. Int. 103 (2016) 1–11.

[88] Y. Ye, D. Zhang, J. Li, T. Liu, J. Pu, H. Zhao, L. Wang, One-step synthesis of superhydrophobic polyhedral oligomeric silsesquioxane-graphene oxide and its application in anti-corrosion and anti-wear fields, Corros. Sci. 147 (2019) 9–21.

[89] S. Hironaka, T. Hayashi, Y. Ohta, Antiwear property of sericite-added grease, Journal of The Japan Petroleum Institute 31 (1988) 507–510.

[90] K. Oshita, S. Komiyama, S. Sasaki, Preparation of a mica–organic hybrid solid lubricant and characterization of its lubrication mechanisms, Tribol. Int. 123 (2018) 349–358.

[91] G. Xu, X. Shen, Fabrication of SiO2 nanoparticles incorporated coating onto titanium substrates by the micro arc oxidation to improve the wear resistance, Surf. Coat. Technol. 364 (2019) 180–186.
[92] M. Aliofkhazraei, R.S. Gharabagh, M. Teimouri, M. Ahmadzadeh, G.B. Darband, H. Hasannejad, Ceria embedded nanocomposite coating fabricated by plasma electrolytic oxidation on titanium, J. Alloy. Compd. 685 (2016) 376–383.
[93] X.-J. Li, M. Zhang, S. Wen, X. Mao, W.-G. Huo, Y.-Y. Guo, Y.-X. Wang, Microstructure and wear resistance of micro-arc oxidation ceramic coatings prepared on 2A50 aluminum alloys, Surf. Coat. Technol. 394 (2020), 125853.

Supplementary materials

Figure S1. Nyquist, bode-impedance and bode-phase angle plots of (a-c) 2024 Al substrate; (d-f) M; (g-i) M-5; (j-l) M-10; (m-o) M-15 after immersion in 3.5 wt% NaCl for 1, 2, 3, and 5 days.

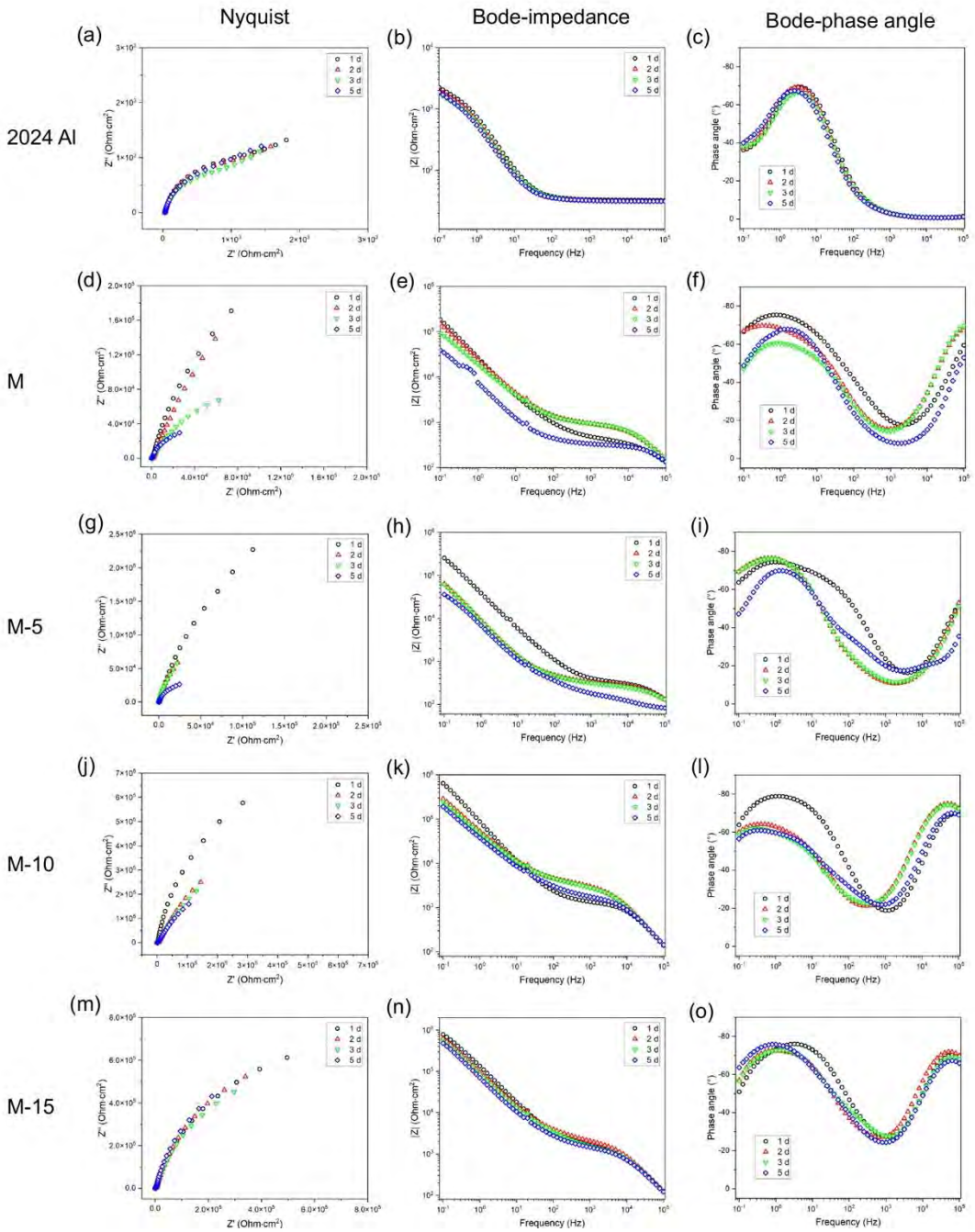

Figure S1